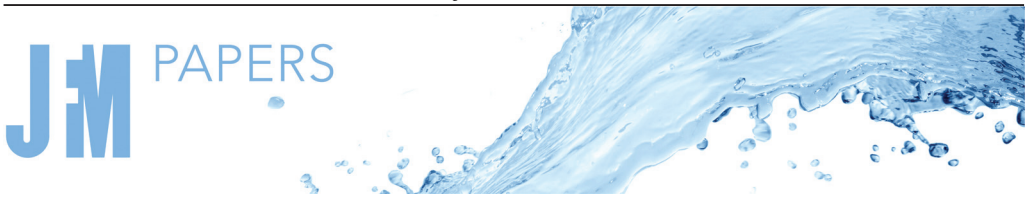
J. Fluid Mech. (2021), *vol*. 927, A27, doi:10.1017/jfm.2021.773



Large-scale characteristics of a stably stratified turbulent shear layer

Tomoaki Watanabe[1],† **and Koji Nagata**[1]

[1]Department of Aerospace Engineering, Nagoya University, Nagoya 464-8603, Japan

(Received 20 November 2020; revised 24 July 2021; accepted 24 August 2021)

Implicit large eddy simulation is performed to investigate large-scale characteristics of a temporally evolving, stably stratified turbulent shear layer arising from the Kelvin–Helmholtz instability. The shear layer at late time has two energy-containing length scales: the scale of the shear layer thickness, which characterizes large-scale motions (LSM) of the shear layer; and the larger streamwise scale of elongated large-scale structures (ELSS), which increases with time. The ELSS forms in the middle of the shear layer when the Richardson number is sufficiently large. The contribution of the ELSS to velocity and density variances becomes relatively important with time although the LSM dominate the momentum and density transport. The ELSS have a highly anisotropic Reynolds stress, to a degree similar to the near-wall region of turbulent boundary layers, while the Reynolds stress of the LSM is as anisotropic as in the outer region. Peaks in the spectral energy density associated with the ELSS emerge because of the slow decay of turbulence at very large scales. A forward interscale energy transfer from large to small scales occurs even at a small buoyancy Reynolds number. However, an inverse transfer also occurs for the energy of spanwise velocity. Negative production of streamwise velocity and density spectra, i.e. counter-gradient transport of momentum and density, is found at small scales. These behaviours are consistent with channel flows, indicating similar flow dynamics in the stratified shear layer and wall-bounded shear flows. The structure function exhibits a logarithmic law at large scales, implying a k^{-1} scaling of energy spectra.

Key words: stratified turbulence, shear layers

1. Introduction

Turbulence in the natural environment is often generated under the influence of vertical shear of large-scale currents. The shear can cause Kelvin–Helmholtz instability, which makes a significant contribution to the transport of momentum and scalar in the flow (Smyth & Moum 2012). Shear flows with stable density stratification are commonly

† Email address for correspondence: watanabe.tomoaki@c.nagoya-u.jp

© The Author(s), 2021. Published by Cambridge University Press

https://doi.org/10.1017/jfm.2021.773 Published online by Cambridge University Press

encountered in geophysical problems, such as the ocean mixing layer (Thorpe 1978) and the atmospheric boundary layer (Mahrt 1999). Therefore, turbulence under the influence of both shear and stable stratification has been studied by many researchers. One of the most simple examples of such turbulent flows is a stably stratified shear layer, which has been studied with both numerical simulations and laboratory experiments. Even under the stable stratification, the Kelvin–Helmholtz instability can produce turbulence when the shear is sufficiently strong (Strang & Fernando 2001). The Kelvin–Helmholtz billows can lead to secondary instabilities, which result in three-dimensional, fully developed turbulence (Klaassen & Peltier 1991). Once the fully developed turbulence is formed in the stably stratified shear layer, the turbulence begins to decay because of the viscous dissipation of turbulent kinetic energy under the stable stratification (Smyth & Moum 2000*b*; Pham & Sarkar 2010). Visualization of the stably stratified shear layer showed that hairpin vortices and highly elongated structures with positive and negative velocity fluctuations appear after the turbulence decays significantly (Watanabe *et al.* 2019*a*). These structures resemble turbulent structures found in wall turbulence. The hairpin vortices were also found in other stably stratified turbulence, e.g. turbulence arising from a breaking internal gravity wave (Fritts, Arendt & Andreassen 1998) and turbulent Holmboe waves (Smyth & Winters 2003).

Three-dimensional direct numerical simulations (DNS) have been utilized to study the stably stratified shear layer. Direct numerical simulation studies often consider a temporally evolving, stably stratified shear layer with localized shear and stratification, where both velocity and density vary sharply across the layer. The flow develops with time in a computational domain that is periodic in the streamwise direction. This flow is often studied as an idealized problem of geophysical flows because a vertical profile of density in DNS resembles a density profile observed in turbulent patches in the ocean thermocline (Smyth & Moum 2000*b*). Direct numerical simulations of temporally evolving shear flows often have a problem in dealing with statistical convergence since the statistics are defined with spatial averages in homogeneous directions (Redford, Lund & Coleman 2015). The degree of statistical convergence depends on the size of the domain in homogeneous directions. Taking ensemble averages from different simulations also improves the convergence. However, because of the limited computational resource and the demand for simulating high-Reynolds-number flows, statistics are often calculated from a single run of DNS with a small domain (da Silva & Pereira 2008; Kozul, Chung & Monty 2016; Watanabe, Zhang & Nagata 2019*b*). Direct numerical simulations of temporally evolving, stratified shear layers have often been conducted with a computational domain which contains several Kelvin–Helmholtz billows (Smyth & Moum 2000*b*). Direct numerical simulations with such a small domain do not provide well-converged statistics, especially for high-order moments.

Another problem in DNS of temporally evolving turbulent flows is a confinement effect due to finite domain size. Recent DNS of a stratified shear layer with a very large domain found elongated large-scale structures (ELSS), whose streamwise length is much larger than the shear layer thickness (Watanabe *et al.* 2019*a*). Most DNS studies in the existing literature could not observe the ELSS because of the limited size of the domain, where fluid motion at large scales is influenced by the boundary conditions. The interaction of fluid motions with different length scales, such as an energy transfer across the scales, is important in turbulent flows, and the confinement effect on large scales can also affect small-scale characteristics. Direct numerical simulations of stably stratified turbulence has been used to evaluate important parameters in oceanography, such as mixing efficiency and turbulent Prandtl number (Peltier & Caulfield 2003; Rahmani, Lawrence & Seymour

https://doi.org/10.1017/jfm.2021.773 Published online by Cambridge University Press

2014; Salehipour & Peltier 2015; Taylor *et al.* 2019). If the ELSS are dynamically important in the flow development, these findings based on DNS with a small domain can also be influenced by the confinement effects.

The typical large-scale structures in turbulent free shear flows have a length scale close to the transverse length of the flow, such as a momentum thickness of a turbulent mixing layer and a mean velocity halfwidth of a turbulent jet (Pope 2000). In this paper turbulent motions at the transverse length scale of a turbulent shear flow are called large-scale motions (LSM). The LSM in turbulent free shear flows are often visualized as large-scale vortices (Bernal & Roshko 1986; Taveira & da Silva 2013). The wavenumber range corresponding to the shear layer thickness has a significant contribution to the turbulent kinetic energy in the stably stratified shear layer (Watanabe *et al.* 2019*a*). Thus, the LSM also exists in the stably stratified shear layer. The ELSS can be distinguished from the LSM by the characteristic length because the ELSS grow much larger than the shear layer thickness. However, the LSM in the stably stratified shear layer is not clearly visible in flow visualization when the LSM coexists with the ELSS. Visualization of the LSM might require an adequate flow decomposition such as a proper orthogonal decomposition (Berkooz, Holmes & Lumley 1993).

The purpose of this study is to investigate the statistical properties at large scales of the stably stratified shear layer with a special focus on LSM and ELSS. Although the ELSS in a stably stratified shear layer are found with flow visualization in Watanabe *et al.* (2019*a*), the dynamical properties of the ELSS are hardly known so far. It is of great interest to elucidate the generation mechanism of ELSS in turbulence research as similar structures also exist in wall turbulence (Nickels *et al.* 2005). The spectral energy budget is analysed in this study to identify the physical processes that contribute to the growth of the velocity and density fluctuations associated with the ELSS. This analysis will be useful to construct a physical model for the generation mechanism of the ELSS in future works. The statistical properties of LSM and ELSS are also investigated by spectral analysis. Since structures similar to the ELSS also exist in wall turbulence, the stably stratified shear layer is compared with turbulent boundary layers and channel flows. Furthermore, the scalings of energy spectra and second-order velocity structure functions at large scales are discussed based on the scalings in wall turbulence.

For this purpose, we perform a well-resolved large eddy simulation (LES) of a temporally evolving, stably stratified shear layer. The LES relies on an implicit subgrid scale (SGS) model, where a filtering scheme accounts for the dissipation at unresolved scales. This approach is often called implicit LES. It has been proved that implicit LES can accurately predict large-scale flow characteristics in various turbulent flows (Bogey & Bailly 2009; Diamessis, Spedding & Domaradzki 2011; Watanabe *et al.* 2019*b*). Furthermore, the turbulent kinetic energy budget in implicit LES was shown to be consistent with DNS and experimental results (Bogey & Bailly 2009; Watanabe *et al.* 2016*b*). The LES conducted in this study is validated by comparison with DNS of the same flow. The low computational cost of LES enables us to repeatedly conduct the simulations for taking ensemble averages. Most statistics presented in this paper are difficult to accurately assess with a single run of DNS or LES because of insufficient statistical convergence. The methodologies of LES and DNS are described in § 2, where the energy budget equations in wavenumber space are also presented for velocity and density fluctuations in LES. Section 3 presents the results of LES, including the validation, the energy budgets and the scale dependence of statistics. Finally, the paper is summarized in § 4.

https://doi.org/10.1017/jfm.2021.773 Published online by Cambridge University Press

2. Implicit LES and DNS of a stably stratified shear layer

2.1. *Temporally evolving, stably stratified shear layer*

Implicit LES and DNS are performed for a temporally evolving, stably stratified shear layer with localized shear and stratification (figure 1), which has also been studied in the existing literature (Smyth & Moum 2000*b*; Mashayek & Peltier 2012; Watanabe, Riley & Nagata 2017). The Navier–Stokes equations with the Boussinesq approximation are used as the governing equations. The density field is expressed by $\rho_a + \rho(x, y, z; t)$ with a constant reference density ρ_a and the deviation from ρ_a denoted by ρ. The flow is statistically homogeneous in the streamwise (x) and spanwise (y) directions, for which periodic boundary conditions are applied. The computational boundaries in the vertical (z) direction are treated with the free-slip boundary conditions for velocity and with the zero-gradient condition in the boundary normal direction for density and pressure. The streamwise velocity and density differences across the stably stratified shear layer are denoted by U_0 and ρ_0 while h_0 is the initial layer thickness. Position x_i, time t, velocity u_i, pressure p and density ρ are non-dimensionalized as

$$x_i = \frac{\tilde{x}_i}{h_0}; \quad t = \frac{\tilde{t}}{t_r}; \quad u_i = \frac{\tilde{u}_i}{U_0}; \quad p = \frac{\tilde{p}}{\rho_a U_0^2}; \quad \rho = \frac{\tilde{\rho}}{\rho_0}. \tag{2.1a–e}$$

Here, $\tilde{f}$ denotes a variable f with dimension and the reference time scale is defined as $t_r = h_0/U_0$. For convenience, $i = 1, 2$ and 3 represent the streamwise, spanwise and vertical components of vectors, where the velocity components in these directions are denoted by u, v and w. The non-dimensionalized governing equations are written as

$$\frac{\partial u_j}{\partial x_j} = 0, \tag{2.2}$$

$$\frac{\partial u_i}{\partial t} + \frac{\partial u_i u_j}{\partial x_j} = -\frac{\partial p}{\partial x_i} + \frac{1}{Re}\frac{\partial^2 u_i}{\partial x_j \partial x_j} - Ri\rho\delta_{i3}, \tag{2.3}$$

$$\frac{\partial \rho}{\partial t} + \frac{\partial u_j \rho}{\partial x_j} = \frac{1}{RePr}\frac{\partial^2 \rho}{\partial x_j \partial x_j}, \tag{2.4}$$

where successive indices imply summation. No external forcing is applied in the flow. The Reynolds number Re, Richardson number Ri and Prandtl number Pr are defined as

$$Re = \frac{U_0 h_0}{\nu}; \quad Ri = \frac{g\rho_0 h_0}{\rho_a U_0^2}; \quad Pr = \frac{\nu}{\kappa}. \tag{2.5a–c}$$

Here, ν is the kinematic viscosity, κ is the diffusivity coefficient for density, g is the gravitational acceleration and δ_{ij} is the Kronecker delta. In previous studies, halves of the shear layer thickness ($h_0/2$) and the velocity jump ($U_0/2$) were also used to define the Reynolds number, which is written as $(h_0/2)(U_0/2)/\nu = Re/4$ (Salehipour & Peltier 2015). The Reynolds number used in this study should be multiplied by 1/4 for comparison with those studies.

The flow is statistically homogeneous in the horizontal directions. Therefore, statistics are defined with an x–y average. The average of a variable $f(x, y, z, t)$, $\langle f \rangle$, is obtained as a

https://doi.org/10.1017/jfm.2021.773 Published online by Cambridge University Press

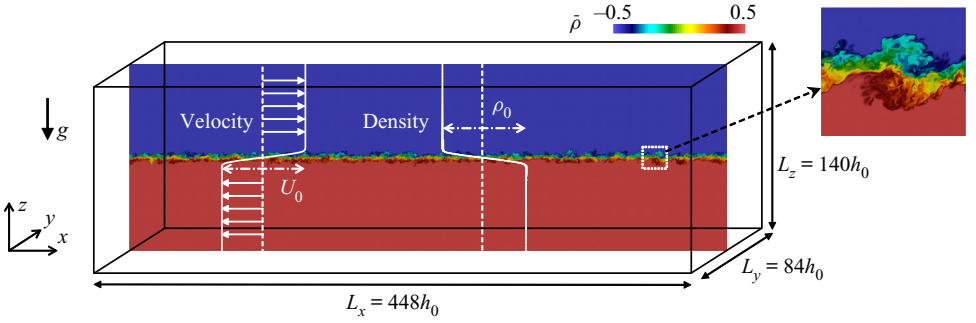


Figure 1. Schematic diagram of numerical simulations of a temporally evolving, stably stratified shear layer.

function of (z, t),

$$\langle f\rangle(z,t) = \frac{1}{L_x L_y}\int_0^{L_y}\int_0^{L_x} f(x,y,z,t)\,\mathrm{d}x\,\mathrm{d}y, \tag{2.6}$$

where L_x and L_y are the sidelengths of the computational domain in the x and y directions. Ensemble averages of repeated simulations are also taken for improving the convergence. Fluctuations of f from the average are denoted by $f'(x,y,z,t) = f(x,y,z,t) - \langle f\rangle(z,t)$, and the root-mean-square (r.m.s.) of the fluctuations is calculated as $f_{rms}(z,t) = (\langle f^2\rangle - \langle f\rangle^2)^{1/2}$. In this study the energy spectra of velocity and density fluctuations are calculated with Fourier transform in the x direction because the LSM and ELSS can be distinguished by their streamwise length scales. Fourier transform of $f(x,y,z,t)$ and its complex conjugate are denoted by $\hat{f}(k_x,y,z,t)$ and $\hat{f}^*(k_x,y,z,t)$, respectively, where k_x is the streamwise wavenumber. An energy spectrum of velocity u_α is defined as $E_{u_\alpha} = \mathrm{Re}[\langle \widehat{u'_\alpha}\widehat{u'_\alpha}^*\rangle]$, where $\mathrm{Re}[\hat{f}]$ represents a real part of $\hat{f}$. Hereafter, Greek subscript letters indicate that no summation is taken over the subscripts. Similarly, a density spectrum is defined as $E_\rho(k_x,z,t) = \mathrm{Re}[\langle \widehat{\rho'}\widehat{\rho'}^*\rangle]$. Here, the spectra are evaluated with the average in the y direction and the ensemble average of repeated simulations.

Following Smyth & Moum (2000*b*), the initial profiles of density and mean streamwise velocity are given by

$$\tilde{\rho} = -0.5\rho_0 \tanh(2\tilde{z}/h_0), \tag{2.7}$$

$$\langle\tilde{u}\rangle = 0.5U_0 \tanh(2\tilde{z}/h_0). \tag{2.8}$$

The mean velocity components in other directions are 0. The initial density field does not have any fluctuations. Artificial velocity fluctuations are superimposed to the mean velocity for $|\tilde{z}| \leqslant h_0/2$ in order to trigger the turbulent transition of the shear layer. As explained below, DNS and LES are repeated with different initial velocity fluctuations to take ensemble averages. The fluctuations are generated with random numbers by the method described in Watanabe *et al.* (2019*b*). In this method, spatially correlated random velocity fluctuations are produced with a grid that discretizes the computational domain with a spacing of Δ_{in}. When three components of the velocity vector at each grid point are given by uniform random numbers, the characteristic length scale of velocity fluctuations is proportional to Δ_{in} (Kempf, Klein & Janicka 2005). Therefore, the length scale can be controlled by changing the non-dimensional grid size Δ_{in}, which is set as $\Delta_{in} = 0.35$. Velocity fluctuations in the x, y and z directions at each grid point are given by the uniform random numbers between -1 and 1. The fluctuations defined on this grid are interpolated

https://doi.org/10.1017/jfm.2021.773 Published online by Cambridge University Press

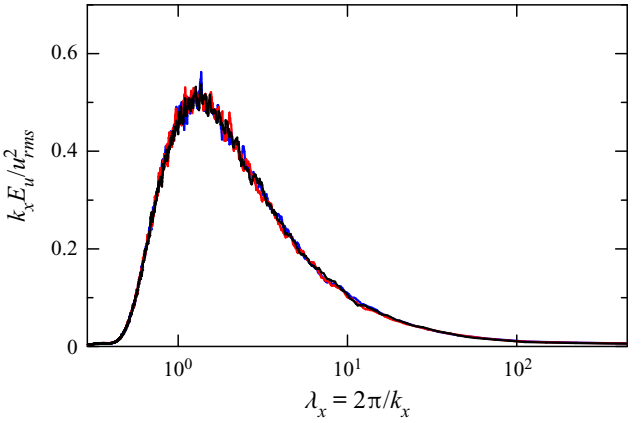


Figure 2. Premultiplied energy spectrum $k_x E_u$ of initial streamwise velocity fluctuations in three simulations of run 2. The spectrum E_u is calculated with Fourier transform in the x direction, and is plotted against the wavelength $\lambda_x = 2\pi/k_x$. Here, $k_x E_u$ is normalized with the r.m.s. of velocity fluctuations u_{rms}.

onto the grid used in DNS or LES with trilinear interpolation. The velocity fluctuations are normalized such that the r.m.s. values normalized by U_0 are equal to 0.012, which is small enough for the roller vortices of the Kelvin–Helmholtz instability to grow. If the initial velocity fluctuations are too strong, the roller vortices do not appear (Kaminski & Smyth 2019). Figure 2 shows the energy spectrum of initial streamwise velocity fluctuations, calculated with the Fourier transform in the x direction. Here, $\lambda_x = 2\pi/k_x$ is the wavelength. Different lines are obtained from three sets of random numbers, which are generated by using a different random seed in a pseudorandom number generator. In this plot, the visible area under the curve of $k_x E_u$ represents the contribution to the velocity variance from a given wavelength (§ 3.3 provides further detailed explanations on the interpretation of the premultiplied spectrum). A peak of $k_x E_u$ is found at $\lambda_x \approx 1.2$, which is the energy-containing length scale of the initial fluctuations. The spectrum hardly varies among the three simulations, and the initial fluctuations are statistically identical among all repeated simulations.

2.2. *Direct numerical simulation*

The DNS code used in this study is based on a fractional step method with finite difference schemes. Variables are stored on a staggered grid, whose spacing is uniform in the horizontal direction and non-uniform in the vertical direction. Spatial derivatives are calculated with fully conservative finite difference schemes (Morinishi *et al.* 1998), where fourth-order and second-order schemes are used in the horizontal and vertical directions, respectively. The low-order schemes require more grid points to achieve the same effective spatial resolution as higher-order schemes. However, these low-order schemes have an advantage in the conservation properties. The fourth-order central difference applied on a uniform grid strictly conserves momentum and kinetic energy. The second-order scheme is also fully conservative even on a non-uniform grid, which is used in the vertical direction. On the other hand, higher-order schemes often violate the conservation laws. The same schemes are used in LES as explained below and these conservation properties are important in LES with a coarse grid. Time is advanced with a third-order Runge–Kutta method. The biconjugate gradient stabilized (Bi-CGSTAB) method is used to solve the Poisson equation for pressure. The same code was also used in our previous studies on

https://doi.org/10.1017/jfm.2021.773 Published online by Cambridge University Press

turbulent shear flows (Watanabe *et al.* 2019*b*), where the DNS results were compared well with experimental and other DNS studies.

2.3. *Implicit LES*

Large eddy simulation is performed with a coarse computational grid which is not fine enough to resolve fluctuations of all length scales existing in the flow. A variable f can be decomposed as $\bar{f} + f''$, where $\bar{f}$ is a grid-scale component that can be expressed on the LES grid while f'' is an SGS component. Large eddy simulation numerically solves governing equations for grid-scale components given by

$$\frac{\partial \bar{u}_j}{\partial x_j} = 0, \tag{2.9}$$

$$\frac{\partial \bar{u}_i}{\partial t} + \frac{\partial \bar{u}_i \bar{u}_j}{\partial x_j} = -\frac{\partial \bar{p}}{\partial x_i} + \frac{1}{Re}\frac{\partial^2 \bar{u}_i}{\partial x_j \partial x_j} - Ri\bar{\rho}\delta_{i3} + R_{u_i}, \tag{2.10}$$

$$\frac{\partial \bar{\rho}}{\partial t} + \frac{\partial \bar{u}_j \bar{\rho}}{\partial x_j} = \frac{1}{RePr}\frac{\partial^2 \bar{\rho}}{\partial x_j \partial x_j} + R_\rho, \tag{2.11}$$

where R_{u_i} and R_ρ are terms associated with the SGS. Here, the mathematical expressions of R_{u_i} and R_ρ are not required in the simulation as they are implicitly modelled in the implicit LES. In this study, R_{u_i} and R_ρ are approximated with a low-pass filter applied to $\bar{u}_i$ and $\bar{\rho}$, where the filter adds artificial dissipation of velocity and density fluctuations. The filter accounts for the dissipation in the SGS (Bogey & Bailly 2009; Watanabe *et al.* 2016*b*).

The LES code used in this study was developed based on the DNS code described above. The SGS terms are implicitly modelled with a tenth-order low-pass filter proposed in Kennedy & Carpenter (1994). The filter is applied to $\bar{u}_i$ and $\bar{\rho}$ at the end of every computational time step. Numerical schemes except for the filter are the same as those used in the DNS. This LES code was also used for implicit LES of turbulent planar jets and turbulent boundary layers with a passive scalar transfer, where the code was validated by comparison with DNS and experiments (Tanaka, Watanabe & Nagata 2019; Watanabe *et al.* 2019*b*).

For the post process of LES data, a filtering operator F is introduced by assuming that the low-pass filter used as the implicit SGS model changes a variable f to $F(f)$. Then, the modelled SGS terms can be explicitly written as

$$R_{u_i} = \frac{F(\bar{u}_i) - \bar{u}_i}{\Delta t}, \quad R_\rho = \frac{F(\bar{\rho}) - \bar{\rho}}{\Delta t}, \tag{2.12a,b}$$

with a time increment Δt of the simulation. These expressions are useful to derive governing equations for various physical quantities, e.g. turbulent kinetic energy and scalar variance, in implicit LES (Bogey & Bailly 2009; Tai, Watanabe & Nagata 2020). Equations (2.12*a*,*b*) are used for the analysis of the energy budgets of velocity and density fluctuations, where F appears in the SGS dissipation terms.

2.4. *Flow and computational parameters*

All DNS and LES are conducted with the domain size $(L_x, L_y, L_z) = (448, 84, 140)$. The number of grid points is $(N_x, N_y, N_z) = (12\,288, 2304, 1200)$ in DNS and (3072, 576, 700) in LES. Table 1 summarizes DNS and LES conducted in this study. The size of the

https://doi.org/10.1017/jfm.2021.773 Published online by Cambridge University Press

Run		Re	Ri	Pr	N_S	Δ_x	Δ_y	Δ_z at $z = 0$	Δ_z at $z = \delta_u/2$
1	DNS	2000	0.06	1	5	0.036	0.036	0.039	0.041
2	LES	2000	0.06	1	35	0.15	0.15	0.066	0.070
3	LES	40 000	0	1	2	0.15	0.15	0.066	0.11
4	LES	40 000	0.02	1	2	0.15	0.15	0.066	0.074
5	LES	40 000	0.06	1	2	0.15	0.15	0.066	0.069
6	LES	40 000	0.1	1	2	0.15	0.15	0.066	0.068

Table 1. Parameters of DNS and LES. Grid sizes Δ_x and Δ_y are constant while Δ_z varies as a function of z. Table presents Δ_z at $z = 0$ and $\delta_u/2$, where δ_u is the shear layer thickness at $t = 320$. The number of simulations repeated with different initial velocity fluctuations is denoted by N_S.

computational domain is large enough for ELSS to grow (Watanabe *et al.* 2019*a*). Both DNS and LES are performed for $(Re, Ri, Pr) = (2000, 0.06, 1)$ (runs 1 and 2). Furthermore, LES is also performed for $Re = 40\,000$ and $Pr = 1$ with $Ri = 0$, 0.02, 0.06 and 0.1 (runs 3–6). For these Re and Ri, the turbulent transition is caused by the Kelvin–Helmholtz instability. The same resolution is used for both $Re = 2000$ and 40 000. This is because the length scale of large-scale fluctuations in the turbulent shear layer is related to h_0 rather than Re. A range of unresolved scales is wider for $Re = 40\,000$ than for $Re = 2000$ because the Kolmogorov scale becomes small as Re increases. For $Ri = 0$, the shear layer thickness monotonically increases with time. It is known that turbulence bounded by an irrotational flow induces large-scale velocity fluctuations outside the turbulent region (Taveira & da Silva 2013; Watanabe, da Silva & Nagata 2020) Therefore, velocity fluctuations are generated even far away from the turbulent shear layer. The very tall domain is used to prevent the confinement effects on the shear layer development and the velocity fluctuations outside the shear layer at $Ri = 0$. Each simulation is repeated N_S times by using different initial velocity fluctuations. Ensemble averages of statistics obtained in each simulation are taken for N_S simulations. The flow is statistically symmetric with respect to z, and most statistics are presented for $z \geqslant 0$. Quantitative analyses with Fourier transform are presented for run 2 because many ensembles are required to obtain well-converged statistics of large-scale quantities. Runs 3–6 are used to examine Ri dependence at high Re. Direct numerical simulation (run 1) is used to validate LES by comparison with run 2. Here, DNS reported in previous studies are not used for the validation because those DNS were conducted with a much smaller computational domain than the present simulations. Appendix A examines the confinement effects due to the finite domain size and shows that the computational domain used in previous studies can significantly affect the turbulent transition and the statistics of velocity and density.

The time increment Δt is $0.02t_r$ in LES and $0.01t_r$ in DNS. The grid spacing is uniform in the streamwise and spanwise directions while the vertical location of the grid points is determined by

$$z(k) = -\frac{L_z}{2\alpha_z}\mathrm{atanh}\left[(\tanh\alpha_z)\left(1 - 2\left(\frac{k-1}{N_z - 1}\right)\right)\right], \tag{2.13}$$

with integers $k = 1, \ldots, N_z$ and the grid stretching parameter $\alpha_z = 3$, where atanh is an inverse hyperbolic tangent function. Equation (2.13) is used in this study because the grid size distribution is symmetric with respect to $z = 0$ and the grid size increases with $|z|$. Compared with the DNS, the grid sizes in the LES are 4 times and 1.7 times larger in the horizontal and vertical directions, respectively. Table 1 presents the grid sizes Δ_i in

https://doi.org/10.1017/jfm.2021.773 Published online by Cambridge University Press

three directions, where Δ_i is non-dimensionalized by h_0. Here, Δ_z is taken at $z = 0$ and at the edge of the shear layer $z = \delta_u/2$ at the end of the simulations ($t = 320$), where $\delta_u(t)$ is the shear layer thickness defined in § 3.2. The vertical distribution of Δ_z for (2.13) can be found in Watanabe *et al.* (2018). The characteristic length of large-scale velocity fluctuations depends on time in the shear layer. At the beginning of the simulation, this length is the initial shear layer thickness h_0 because the initial roller vortices arising from the instability have a diameter with $O(h_0)$. After the turbulent transition, the vertical width of the turbulent shear layer, which is larger than h_0, characterizes large-scale fluctuations. Therefore, as long as the LES resolves h_0, the LES has a sufficient resolution to resolve the large-scale fluctuations even after the turbulent shear layer has fully developed. The number of grid points is determined so that $\Delta_i \ll 1$ is satisfied. Although the LES grid resolves most length scales in run 2, the implicit SGS model is necessary because well-resolved LES without the SGS model results in an unphysical growth of energy at small scales, which affects the shape of energy spectra (Watanabe *et al.* 2019*b*).

2.5. *Spectral budget equations for turbulent kinetic energy and density variance in LES*

The scale dependence of the budget of turbulent kinetic energy and density variance is studied with Fourier transform in the x direction. The governing equations for the energy spectra of velocity and density are presented for implicit LES in this section. Applying a Fourier transform to the equations for $\bar{u}'_\alpha$ yields the equations for $\widehat{\bar{u}'_\alpha}$. One can multiply the equations for $\widehat{\bar{u}'_\alpha}$ by $\widehat{\bar{u}'_\alpha}^*$ and take an average in order to derive the budget equations for E_{u_α} (Mizuno 2016). The transport equation for E_{u_α} in implicit LES is written as

$$\frac{\partial E_{u_\alpha}/2}{\partial t} + \langle \bar{u}_j \rangle \frac{\partial E_{u_\alpha}/2}{\partial x_j} = \hat{P}^{(u_\alpha)} + \hat{\Pi}^{(u_\alpha)} + \hat{T}_P^{(u_\alpha)} + \hat{T}_T^{(u_\alpha)} + \hat{D}^{(u_\alpha)} + \hat{T}_S^{(u_\alpha)} + \hat{B}^{(u_\alpha)} - \hat{\varepsilon}_G^{(u_\alpha)} - \hat{\varepsilon}_S^{(u_\alpha)}, \tag{2.14}$$

with

$$\left.\begin{aligned}
\hat{P}^{(u_\alpha)} &= \mathrm{Re}\left[-\left\langle \widehat{\bar{u}'_\alpha}^* \widehat{\bar{u}'_j} \right\rangle \frac{\partial \langle \bar{u}_\alpha \rangle}{\partial x_j} \right], \quad \hat{\Pi}^{(u_\alpha)} = \mathrm{Re}\left[\left\langle \widehat{p'} \widehat{\frac{\partial \bar{u}'_\alpha}{\partial x_\alpha}}^* \right\rangle \right], \\
\hat{T}_P^{(u_\alpha)} &= \mathrm{Re}\left[-\frac{\partial}{\partial x_\alpha} \left\langle \widehat{p'} \widehat{\bar{u}'_\alpha}^* \right\rangle \right], \quad \hat{T}_T^{(u_\alpha)} = \mathrm{Re}\left[-\left\langle \frac{1}{2} \frac{\partial \widehat{\bar{u}'_\alpha}^* \widehat{\bar{u}'_\alpha \bar{v}'}}{\partial y} + \frac{1}{2} \frac{\partial \widehat{\bar{u}'_\alpha}^* \widehat{\bar{u}'_\alpha \bar{w}'}}{\partial z} \right\rangle \right], \\
\hat{D}^{(u_\alpha)} &= \mathrm{Re}\left[\frac{1}{Re} \frac{\partial^2}{\partial x_j \partial x_j} \left\langle \widehat{\bar{u}'_\alpha} \widehat{\bar{u}'_\alpha}^*/2 \right\rangle \right], \quad \hat{B}^{(u_\alpha)} = \mathrm{Re}\left[-Ri \delta_{\alpha 3} \left\langle \widehat{\bar{u}'_\alpha}^* \widehat{\bar{\rho}'} \right\rangle \right], \\
\hat{\varepsilon}_G^{(u_\alpha)} &= \mathrm{Re}\left[\frac{1}{Re} \left\langle \widehat{\frac{\partial \bar{u}'_\alpha}{\partial x_j}}^* \widehat{\frac{\partial \bar{u}'_\alpha}{\partial x_j}} \right\rangle \right], \quad \hat{\varepsilon}_S^{(u_\alpha)} = -\mathrm{Re}\left[\left\langle \widehat{\bar{u}'_\alpha}^* \widehat{F(\bar{u}'_\alpha)} \right\rangle \right], \\
\hat{T}_S^{(u_\alpha)} &= \mathrm{Re}\left[-\left\langle \widehat{\bar{u}'_\alpha}^* \widehat{\frac{\partial \bar{u}'_\alpha \bar{u}'}{\partial x}} \right\rangle - \left\langle \widehat{\bar{u}'_\alpha}^* \widehat{\frac{\partial \bar{u}'_\alpha \bar{v}'}{\partial y}} + \widehat{\bar{u}'_\alpha}^* \widehat{\frac{\partial \bar{u}'_\alpha \bar{w}'}{\partial z}} \right\rangle \right. \\
&\quad \left. + \left\langle \frac{1}{2} \frac{\partial \widehat{\bar{u}'_\alpha}^* \widehat{\bar{u}'_\alpha \bar{v}'}}{\partial y} + \frac{1}{2} \frac{\partial \widehat{\bar{u}'_\alpha}^* \widehat{\bar{u}'_\alpha \bar{w}'}}{\partial z} \right\rangle \right].
\end{aligned}\right\} \tag{2.15}$$

https://doi.org/10.1017/jfm.2021.773 Published online by Cambridge University Press

These terms are production $\hat{P}^{(u_\alpha)}$, pressure–strain correlation $\hat{\Pi}^{(u_\alpha)}$, pressure diffusion $\hat{T}_P^{(u_\alpha)}$, turbulent transport in physical space $\hat{T}_T^{(u_\alpha)}$, viscous diffusion $\hat{D}^{(u_\alpha)}$, buoyancy flux $\hat{B}^{(u_\alpha)}$, viscous dissipation at the grid scales $\hat{\varepsilon}_G^{(u_\alpha)}$, dissipation due to the implicit SGS model $\hat{\varepsilon}_S^{(u_\alpha)}$ and turbulent transport in the wavenumber space $\hat{T}_S$. The advection term by mean velocity on the left-hand side of (2.14) is zero in the temporally evolving shear layer because $E_{u_\alpha}(k_x, z, t)$ does not depend on x and y and the mean velocity in the z direction is zero. The pressure–strain correlation, $\hat{\Pi}^{(u_\alpha)}$, is the redistribution term of the turbulent kinetic energy among three directions as $\hat{\Pi}^{(u)} + \hat{\Pi}^{(v)} + \hat{\Pi}^{(w)} = 0$. The derivative $\partial/\partial x$ can be written as ik_x in the wavenumber space. However, the derivative calculation in the wavenumber space is not consistent with the numerical schemes of the LES. Therefore, all spatial derivatives in these terms are calculated in the physical space.

Similarly, we can derive the budget equation for the density spectrum E_ρ,

$$\frac{\partial E_\rho/2}{\partial t} + \langle \bar{u}_j \rangle \frac{\partial E_\rho/2}{\partial x_j} = \hat{P}^{(\rho)} + \hat{T}_T^{(\rho)} + \hat{D}^{(\rho)} + \hat{T}_S^{(\rho)} - \hat{\varepsilon}_G^{(\rho)} - \hat{\varepsilon}_S^{(\rho)}, \tag{2.16}$$

with

$$\left.\begin{aligned}
\hat{P}^{(\rho)} &= \mathrm{Re}\left[-\left\langle \hat{\bar{\rho}}^* \widehat{\bar{u}_j'} \right\rangle \frac{\partial \langle \bar{\rho} \rangle}{\partial x_j}\right], \quad \hat{T}_T^{(\rho)} = \mathrm{Re}\left[-\left\langle \frac{1}{2}\frac{\partial \hat{\bar{\rho}}^* \widehat{\bar{\rho}'\bar{v}'}}{\partial y} + \frac{1}{2}\frac{\partial \hat{\bar{\rho}}^* \widehat{\bar{\rho}'\bar{w}'}}{\partial z} \right\rangle\right], \\
\hat{D}^{(\rho)} &= \mathrm{Re}\left[\frac{1}{RePr}\frac{\partial^2}{\partial x_j \partial x_j}\left\langle \hat{\bar{\rho}}\, \hat{\bar{\rho}}^*/2 \right\rangle\right], \quad \hat{\varepsilon}_G^{(\rho)} = \mathrm{Re}\left[\frac{1}{RePr}\left\langle \widehat{\frac{\partial \bar{\rho}'}{\partial x_j}}^* \widehat{\frac{\partial \bar{\rho}'}{\partial x_j}} \right\rangle\right], \\
\hat{\varepsilon}_S^{(\rho)} &= -\mathrm{Re}\left[\left\langle \hat{\bar{\rho}}^* \widehat{F(\bar{\rho}')} \right\rangle\right], \\
\hat{T}_S^{(\rho)} &= \mathrm{Re}\left[-\left\langle \hat{\bar{\rho}}^* \widehat{\frac{\partial \bar{\rho}'\bar{u}'}{\partial x}} \right\rangle - \left\langle \hat{\bar{\rho}}^* \widehat{\frac{\partial \bar{\rho}'\bar{v}'}{\partial y}} + \hat{\bar{\rho}}^* \widehat{\frac{\partial \bar{\rho}'\bar{w}'}{\partial z}} \right\rangle + \left\langle \frac{1}{2}\frac{\partial \hat{\bar{\rho}}^* \widehat{\bar{\rho}'\bar{v}'}}{\partial y} + \frac{1}{2}\frac{\partial \hat{\bar{\rho}}^* \widehat{\bar{\rho}'\bar{w}'}}{\partial z} \right\rangle\right].
\end{aligned}\right\} \tag{2.17}$$

These terms represent production $\hat{P}^{(\rho)}$, turbulent transport in physical space $\hat{T}_T^{(\rho)}$, diffusion $\hat{D}^{(\rho)}$, dissipation at the grid scales $\hat{\varepsilon}_G^{(\rho)}$, dissipation due to the implicit SGS model $\hat{\varepsilon}_S^{(\rho)}$ and turbulent transport in the wavenumber space $\hat{T}_S^{(\rho)}$.

3. Results and discussion

3.1. *Flow visualization*

Figure 3 shows an instantaneous density profile on an x–z plane at $t = 60$ and 200 in run 2. Vortices generated by the Kelvin–Helmholtz instability can be seen in figure 3(*a*). After these vortices collapse, the flow becomes turbulent with small-scale density fluctuations in figure 3(*b*). This temporal development of the stably stratified shear layer agrees well with the previous DNS with the same Reynolds number and Richardson number (Watanabe *et al.* 2019*a*).

Figure 4 visualizes streamwise velocity fluctuations $\bar{u}'$ in run 2 on the horizontal plane at $z = 0$ from $t = 2$ to 320. The characteristic length scale of the velocity fluctuations increases with time. At late time, the velocity distribution is highly anisotropic, and regions with positive and negative $\bar{u}'$ are elongated in the x direction. These are related to the ELSS, which were also found in previous DNS (Watanabe *et al.* 2019*a*). Figure 4(*f*) depicts the

https://doi.org/10.1017/jfm.2021.773 Published online by Cambridge University Press

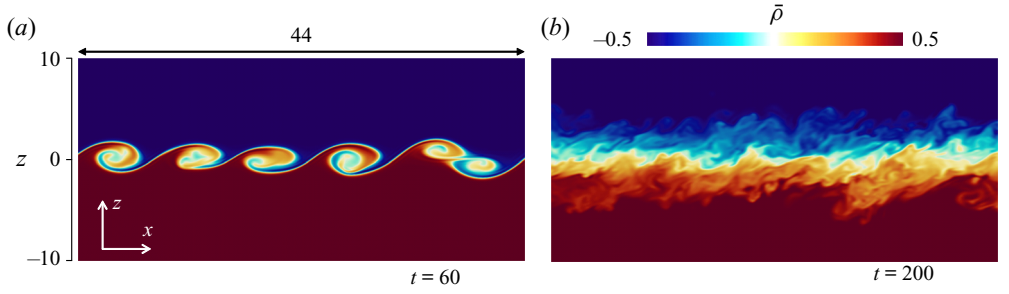


Figure 3. Density $\bar{\rho}$ on an x–z plane at (*a*) $t = 60$ and (*b*) $t = 200$ in run 2. Only a small part of the computational domain is shown here.

length of the shear layer thickness δ_u, which is defined with the mean streamwise velocity $\langle\bar{u}\rangle$ as the vertical distance between $\langle\bar{u}\rangle = -0.49$ and 0.49. The vertical profile of $\langle\bar{u}\rangle$ is presented in the next subsection. The streamwise length of the ELSS is as large as $10\delta_u$ while the spanwise length is about δ_u. The streamwise and spanwise sizes of the ELSS are smaller than L_x and L_y even at $t = 320$, respectively, and the computational domain contains multiple ELSS identified by $\bar{u}'$. The longitudinal auto-correlation functions of u and v are defined as

$$f_u(r_x, z, t) = \langle u'(x, y, z, t)u'(x + r_x, y, z, t)\rangle / u^2_{rms}(z, t), \tag{3.1}$$

$$f_v(r_y, z, t) = \langle v'(x, y, z, t)v'(x, y + r_y, z, t)\rangle / v^2_{rms}(z, t). \tag{3.2}$$

Here, r_i is the distance between two points separated in the i direction. If the domain is small compared with the length scale of the flow, f_u and f_v do not reach zero at large scales because the periodic boundary conditions generate artificial correlation between two points (Davidson 2004). In run 2, $f_u(r_x)$ and $f_v(r_y)$ at $z = 0$ and $t = 320$ reach 0 at $r_x = 41.1$ and $r_y = 8.2$, which are about $L_x/10$ and $L_y/10$, respectively. Thus, the domain is large enough to prevent the finite domain size from affecting the development of turbulence. Velocity fluctuations at $t = 2$ are related to the initial velocity fluctuations. The roller vortices of the Kelvin–Helmholtz instability exist at $t = 60$. The diameter of the roller vortices at $t = 60$ is $O(h_0)$ in figure 3(*a*), and this length is much smaller than the streamwise length of the ELSS, which is as large as $10^2 h_0$. Thus, the velocity fluctuations after $t = 120$ are hardly correlated with those at $t = 2$ and 60.

3.2. *Fundamental statistics of stably stratified shear layers*

The LES is validated by comparison between runs 1 (DNS) and 2 (LES). Figure 5(*a*) compares vertical profiles of mean streamwise velocity and density. These profiles show that the shear layer grows from $t = 100$ to 240 because both mean streamwise velocity (momentum) and density are transferred in the vertical direction by turbulence. Figure 5(*b*) shows the temporal evolution of r.m.s. velocity fluctuations at $z = 0$ and shear layer thickness δ_u. The figure also includes u_{rms} in five LES before the ensemble average is taken. The difference among the five simulations is small, and the domain size is large enough to obtain well-converged statistics for r.m.s. quantities. When the turbulence is generated by the instability, the r.m.s. velocity fluctuations increase with time. The fluctuations begin to decay after they reach a peak. The shear layer thickness also increases at early time. However, the growth of the shear layer thickness becomes slow after $t \approx 150$

https://doi.org/10.1017/jfm.2021.773 Published online by Cambridge University Press

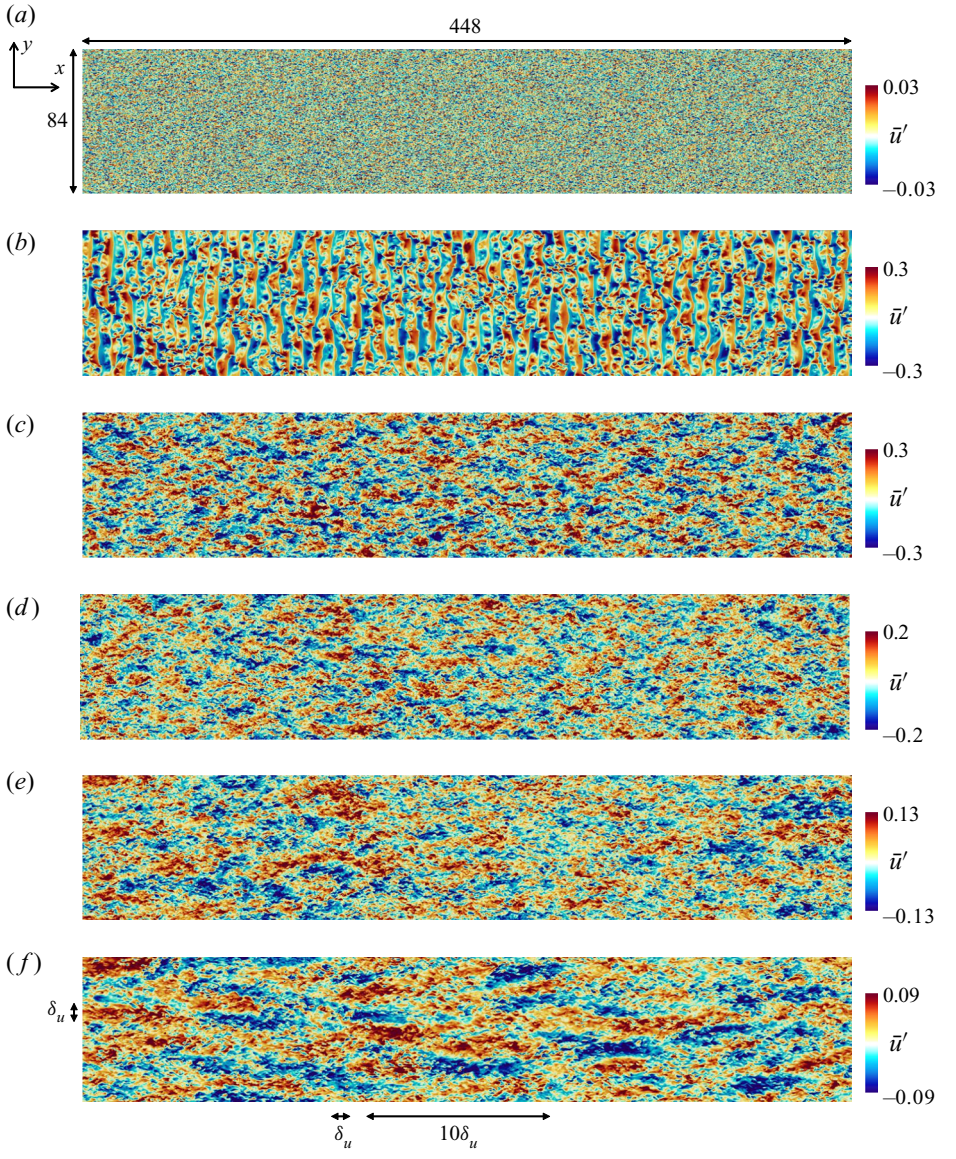


Figure 4. Streamwise velocity fluctuations $\bar{u}'$ on the horizontal plane at the centre of the shear layer in run 2: (*a*) $t = 2$; (*b*) $t = 60$; (*c*) $t = 120$; (*d*) $t = 180$; (*e*) $t = 240$; (*f*) $t = 320$. Figure (*f*) depicts the size of δ_u and $10\delta_u$, where δ_u is the shear layer thickness defined with the mean velocity profile.

because of the stable stratification. These statistics are almost identical between the LES and DNS.

Figure 6(*a*) compares the energy spectrum of streamwise velocity, E_u, between runs 1 and 2. The LES and DNS results agree well with each other for a low wavenumber range while E_u in the LES sharply drops for $k_x \gtrsim 10$. The spectrum at $t = 60$ has a peak at $k_x \approx 0.6$, which is associated with the roller vortices. The wavelength of this peak is $\lambda_x \approx 10$, which is much smaller than the streamwise length of the ELSS at $t = 320$. Therefore, the length scales of large-scale fluctuations are different between the transitional and fully developed states. As also found in figure 4, the velocity fluctuations during the transition

https://doi.org/10.1017/jfm.2021.773 Published online by Cambridge University Press

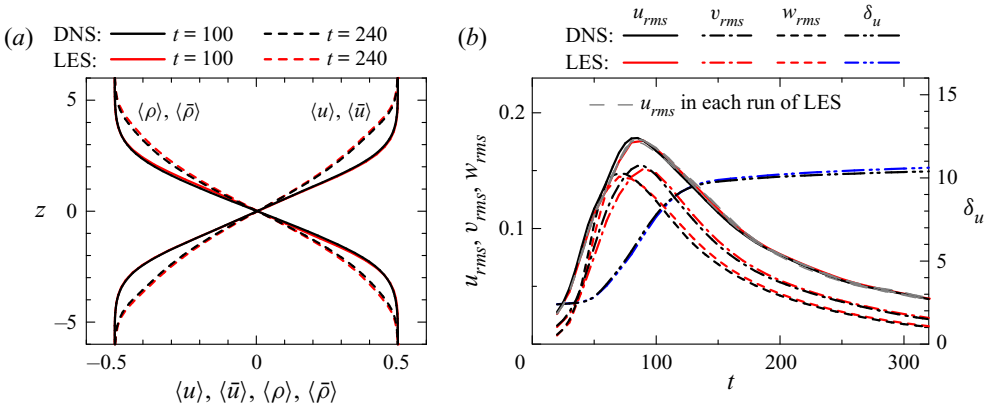


Figure 5. Comparisons between DNS (run 1) and LES (run 2). (*a*) Vertical profiles of mean velocity and density at $t = 100$ and 240. (*b*) Temporal variations of root-mean-squared velocity fluctuations at $z = 0$ and shear layer thickness δ_u. Grey broken lines represent u_{rms} in five simulations of LES.

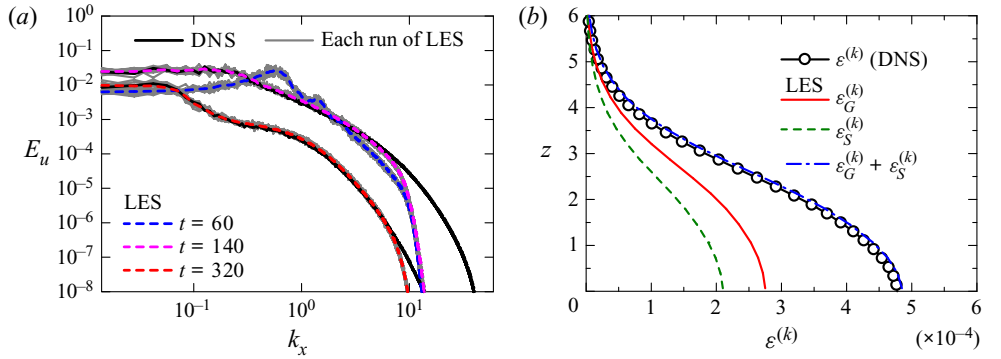


Figure 6. (*a*) Energy spectrum of streamwise velocity E_u at the centre of the shear layer at $t = 60$, 140 and 320 in LES (run 2). Direct numerical simulation results at $t = 140$ and 320 are also shown for comparison. Grey lines are E_u in each simulation of LES (nine simulations). (*b*) Vertical profiles of turbulent kinetic energy dissipation rate at $t = 140$ in DNS ($\varepsilon^{(k)}$ in run 1) and LES ($\varepsilon_G^{(k)} + \varepsilon_S^{(k)}$ in run 2). The dissipation terms of grid scales ($\varepsilon_G^{(k)}$) and subgrid scales ($\varepsilon_S^{(k)}$) are also shown in the figure.

are not directly related to those at late time. The figure also shows E_u obtained in each run of the LES. The shape of E_u at $t = 60$ is qualitatively similar among nine simulations, and the size and spacing of the roller vortices are statistically identical among all simulations. Quantitative variations among different simulations are noticeable for a low wavenumber range, for which the convergence of spectra is improved by taking ensemble averages of 35 simulations.

In implicit LES the dissipation terms of turbulent kinetic energy by the grid scales and the SGS model are given respectively by

$$\varepsilon_G^{(k)} = \frac{1}{Re}\left\langle \frac{\partial \bar{u}_i'}{\partial x_j}\frac{\partial \bar{u}_i'}{\partial x_j}\right\rangle, \quad \varepsilon_S^{(k)} = -\left\langle \bar{u}_i' F(\bar{u}_i')\right\rangle. \tag{3.3a,b}$$

Figure 6(*b*) shows the turbulent kinetic energy dissipation rate at $t = 140$ in runs 1 and 2. The total dissipation rate $\varepsilon_G^{(k)} + \varepsilon_S^{(k)}$ in the LES agrees well with the dissipation rate in

https://doi.org/10.1017/jfm.2021.773 Published online by Cambridge University Press

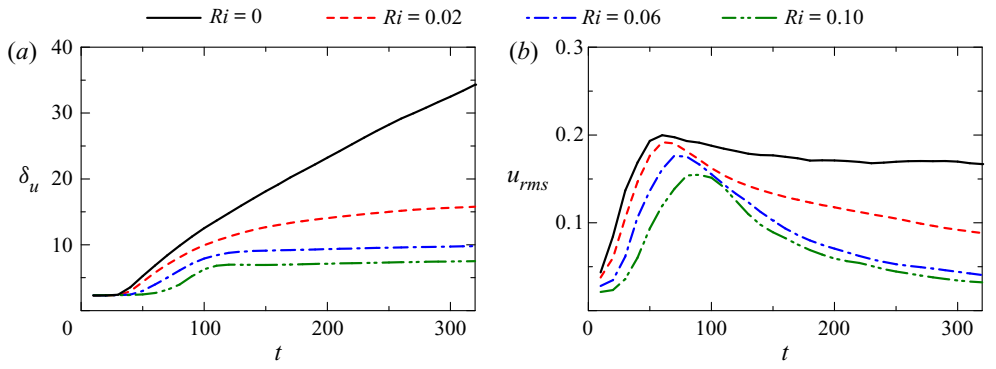


Figure 7. Temporal variations of (a) shear layer thickness δ_u and (b) r.m.s. streamwise velocity fluctuations at $z = 0$ for $Re = 40\,000$ (runs 3–6).

the DNS, which is calculated as $\varepsilon^{(k)} = \varepsilon_G^{(k)}$ by replacing $\bar{u}_i'$ with u_i' in (3.3a,b). Therefore, the amount of dissipation is accurately controlled by the implicit SGS model. In the LES, $\varepsilon_S^{(k)}$ is as large as $\varepsilon_G^{(k)}$, and about one half of the energy dissipation is treated with the model at $t = 140$. The implicit LES does not use the dynamic adjustment of the filter. The averaged energy dissipation rate in turbulence is generally controlled by the averaged interscale energy flux from large to small scales. The filter dissipates the energy at resolved small scales before the energy is transferred to further small scales. The good agreement in the dissipation rate between LES and DNS may be explained by the spatial resolution of LES, which is good enough to resolve large-scale fluctuations that determine the averaged interscale energy flux.

Figure 7(a) shows the temporal evolution of δ_u at $Re = 40\,000$ in runs 3–6. In the non-stratified turbulent shear layer ($Ri = 0$), δ_u almost linearly increases with time for $t \gtrsim 100$. As also found at $Re = 2000$, the growth of δ_u at $Re = 40\,000$ is very slow for $t \gtrsim 150$ at $Ri = 0.06$ and 0.1. However, δ_u at $Ri = 0.02$ gradually increases even for $t \gtrsim 150$. Figure 7(b) shows u_{rms} on the shear layer centreline at $Re = 40\,000$. In a self-similar turbulent mixing layer, u_{rms} at $z = 0$ does not vary with time (Rogers & Moser 1994). Indeed, $u_{rms} \approx 0.17$ at $Ri = 0$ hardly varies after the turbulent shear layer has fully developed, and this value of 0.17 agrees well with previous studies on self-similar turbulent mixing layers (Rogers & Moser 1994). The time of the peak in u_{rms} depends on Ri. Furthermore, comparison of u_{rms} between figures 5(b) and 7(b) also confirms that u_{rms} at $Ri = 0.06$ reaches a peak slightly earlier for $Re = 40\,000$ than for $Re = 2000$. These differences in the initial growth of u_{rms} imply that the detailed transition process depends on Re and Ri.

The comparisons between the DNS and LES confirm that the LES accurately captures large-scale velocity and density fluctuations of the flow. The LES results will be used to assess the statistical properties of the stably stratified shear layer. In the rest of the paper most results are presented for $t = 140$, 240 and 320. Table 2 summarizes important parameters of the flow obtained by LES at these time instances, where $L_O = \sqrt{\varepsilon^{(k)}/N^3}$ is the Ozmidov scale defined with the buoyancy frequency $\tilde{N} = \sqrt{-(g/\rho_a)\langle\partial\tilde{\rho}/\partial\tilde{z}\rangle}$ ($N = \tilde{N}t_r$), $\eta = (Re^3\varepsilon^{(k)})^{-1/4}$ is the Kolmogorov scale, $Re_b = (L_O/\eta)^{4/3}$ is the buoyancy Reynolds number and $Ri_g = N^2/\langle\partial u/\partial z\rangle^2$ is the gradient Richardson number. The turbulent kinetic energy dissipation rate in LES is calculated as $\varepsilon^{(k)} = \varepsilon_G^{(k)} + \varepsilon_S^{(k)}$. The table shows L_O, η, Re_b and Ri_g obtained at $z = 0$. Here, L_O and η are normalized by δ_u

https://doi.org/10.1017/jfm.2021.773 Published online by Cambridge University Press

Re, Ri	Time	L_O/δ_u	η/δ_u	Re_b	Ri_g
	140	6.9×10^{-2}	2.3×10^{-3}	9.3×10^{1}	0.47
2000, 0.06	240	2.5×10^{-2}	3.7×10^{-3}	1.3×10^{1}	0.47
	320	1.2×10^{-2}	5.2×10^{-3}	2.9×10^{0}	0.49
	140	—	1.4×10^{-4}	—	—
40 000, 0	240	—	9.9×10^{-5}	—	—
	320	—	8.4×10^{-5}	—	—
	140	2.2×10^{-1}	2.0×10^{-4}	1.2×10^{4}	0.16
40 000, 0.02	240	1.3×10^{-1}	2.1×10^{-4}	5.1×10^{3}	0.21
	320	9.8×10^{-2}	2.3×10^{-4}	3.2×10^{3}	0.24
	140	6.7×10^{-2}	2.9×10^{-4}	1.4×10^{3}	0.42
40 000, 0.06	240	2.8×10^{-2}	4.3×10^{-4}	2.6×10^{2}	0.44
	320	1.8×10^{-2}	5.3×10^{-4}	1.1×10^{2}	0.46
	140	4.0×10^{-2}	3.7×10^{-4}	5.2×10^{2}	0.51
40 000, 0.1	240	1.3×10^{-2}	6.3×10^{-4}	5.9×10^{1}	0.53
	320	6.1×10^{-3}	9.0×10^{-4}	1.3×10^{1}	0.56

Table 2. Statistical properties of the stably stratified shear layer in LES. Values of L_O, η, Re_b and Ri_g are taken at the centre of the shear layers.

because the energy spectra will be presented as functions of a wavelength normalized by δ_u. In the rest of the paper, z is also normalized by δ_u because z/δ_u is useful to indicate the location with respect to the shear layer thickness. In run 2 the spatial resolution Δ_x is 2.2η-8.0η, where Δ_x/η decreases with time. Thus, most length scales are resolved in run 2, which will be used to evaluate the transport equations of energy spectra. Runs 3–6 have $\Delta_x/\eta = O(10^1)$ and large-scale velocity and density fluctuations are well resolved in LES. The Ozmidov scale is often interpreted as the smallest length scale that is affected by the buoyancy, and it is considered that vertical turbulent motions at scales greater than L_O are significantly damped. The buoyancy Reynolds number is defined as the ratio between L_O and η. As η represents the smallest scale of turbulence, $Re_b \gg 1$ indicates that small-scale turbulent motions are not directly influenced by the stable stratification. This is comfortably the case at $t = 140$ with $Re_b = 93$ for $(Re, Ri) = (2000, 0.06)$. However, smaller values of Re_b at the later time indicate that turbulent motions at the smallest scale are strongly suppressed by the buoyancy. At $Re = 40\,000$, Re_b is larger than $O(10^1)$ except at late time with $Ri = 0.1$. At $Ri = 0.06$ and 0.1, $Ri_g = 0.42$–0.56 weakly depends on time after $t = 140$. On the other hand, Ri_g increases from 0.16 to 0.24 at $(Re, Ri) = (40\,000, 0.02)$ because the shear layer thickness also grows with time.

3.3. *Energy spectra of velocity and density*

The energy spectra of velocity and density fluctuations are calculated with Fourier transform in the x direction. These spectra, premultiplied by the streamwise wavenumber k_x, are plotted against the vertical location z and the streamwise wavelength $\lambda_x = 2\pi/k_x$, where λ_x is shown on a logarithmic scale. When $E_u(k_x)$ at a given vertical position is shown in a linear plot, the visible area beneath the curve between wavenumbers k_{x1} and k_{x2} can be interpreted as the contribution to $\langle u'^2 \rangle$ from $k_{x1} \leqslant k_x \leqslant k_{x2}$ because of $\langle u'^2 \rangle = \int_0^\infty E_u(k_x)\,\mathrm{d}k_x$. The equivalent relation for the logarithmic coordinate of k_x is $\langle u'^2 \rangle = \int_{-\infty}^{\infty} k_x E_u d(\log_{10} k_x)$, which is obtained with $dk_x = k_x d(\log_{10} k_x)$. Therefore, when the spectrum is plotted on the logarithmic coordinate of k_x, $k_x E_u$ is useful because it is

https://doi.org/10.1017/jfm.2021.773 Published online by Cambridge University Press

the contribution to $\langle u'^2 \rangle$ on the coordinate of $\log_{10} k_x$. This meaning of the premultiplied spectrum is held even if $\lambda_x = 2\pi/k_x$ is used instead of k_x because $d \log_{10} k_x$ is proportional to $-d \log_{10} \lambda_x$. As the turbulent kinetic energy is distributed over a wide range of scales, the premultiplied spectrum is widely used to assess the scale dependence of turbulent kinetic energy (Kim & Adrian 1999; Hutchins & Marusic 2007; Takamure *et al.* 2018). Similarly, premultiplied cospectra related to turbulent fluxes of momentum and density have been used in previous studies on stratified turbulent flows (Lienhard & van Atta 1990; Gerz & Schumann 1996; Komori & Nagata 1996).

Figure 8(*a–c*) shows the energy spectrum of streamwise velocity, $k_x E_u$, at $t = 140$, 240 and 320 in run 2. As also observed in previous DNS (Watanabe *et al.* 2019*a*), the spectral shape significantly changes with time. At $t = 140$, $k_x E_u$ at each vertical location has a single peak around $\lambda_x/\delta_u \approx 2$. At late time, the middle of the shear layer has a spectral shape with two peaks at $\lambda_x/\delta_u \approx 1$ and 10 while a single peak can be identified for $z/\delta_u \gtrsim 0.3$. The peak in $k_x E_u$ at $\lambda_x/\delta_u \approx 10$ is related to the ELSS visualized in figure 4(*f*), where regions with positive and negative fluctuations extend over about $10\delta_u$ in the x direction. A similar spectral evolution can be found for E_v and E_w shown in figure 8(*d–i*). Figure 8(*j-l*) shows $k_x E_\rho$ at the same time instances. As found for the kinetic energy spectra, $k_x E_\rho$ in the middle of the shear layer at $t = 320$ has two peaks at $\lambda_x/\delta_u \approx 0.6$ and 8. However, $k_x E_\rho$ decreases with z while the velocity spectra have a large peak at $z/\delta_u \approx 0.4$. These spectral shapes in the LES generally agree with the DNS results in Watanabe *et al.* (2019*a*). However, the peak locations are more clearly identified in the LES since ensemble averages are taken in this study.

The double-peak spectra at late time indicate that the flow in the middle of the shear layer has two energy-containing length scales, which can be identified as the peak wavelengths. One is the short peak-wavelength of the spectra, which is close to the shear layer thickness δ_u. In turbulent free shear flows, such as jets, wakes and mixing layers, a characteristic length of LSM is the width of the flow (Pope 2000). Therefore, the peak at $\lambda_x \sim \delta_u$ is associated with usual LSM, which appear in a turbulent shear layer even without stable stratification. Fluid motions at this length scale are simply referred to as 'LSM'. The other energy-containing length scale is obtained as the long peak-wavelength, which is much larger than δ_u. This length scale is related to the streamwise length of elongated patterns of velocity fluctuations visualized in figure 4(*f*). Therefore, fluid motions associated with fluctuations at the long peak-wavelength are called 'ELSS'.

The peak in $k_x E_u$ associated with the ELSS is found only for $|z|/\delta_u \lesssim 0.3$. The ELSS hardly reach the interfacial region between the turbulent shear layer and the non-turbulent region, which are separated by a thin interfacial layer (turbulent/non-turbulent interface). Visualization of the turbulent/non-turbulent interface in a stably stratified shear layer showed that the interface geometry does not exhibit an imprint of the ELSS (Watanabe, Riley & Nagata 2016*a*). This is because the ELSS appear in the middle of the shear layer while the interface is formed at the outer edge of the shear layer. The ELSS and the interface are separated in space, and it is expected that the ELSS do not have significant influences on the turbulent/non-turbulent interface.

The existence of LSM and ELSS for $Re < 2000$ was reported in Watanabe *et al.* (2019*a*). Runs 3–6 are used to examine them at high Re. Figure 9 shows $k_x E_u$ at $z = 0$ for $Re = 40\,000$. The spectrum $k_x E_u$ is normalized by its maximum value $[k_x E_u]_{max}$ at $z = 0$ in order to compare the plots at different time. The formation of the double-peak spectrum occurs for $Ri = 0.06$ and 0.1. For low Ri, $k_x E_u$ has a single peak and the flow has only one characteristic length scale at large scales. This large single peak is expected from the presence of large-scale roller vortices in a turbulent mixing layer without density

https://doi.org/10.1017/jfm.2021.773 Published online by Cambridge University Press

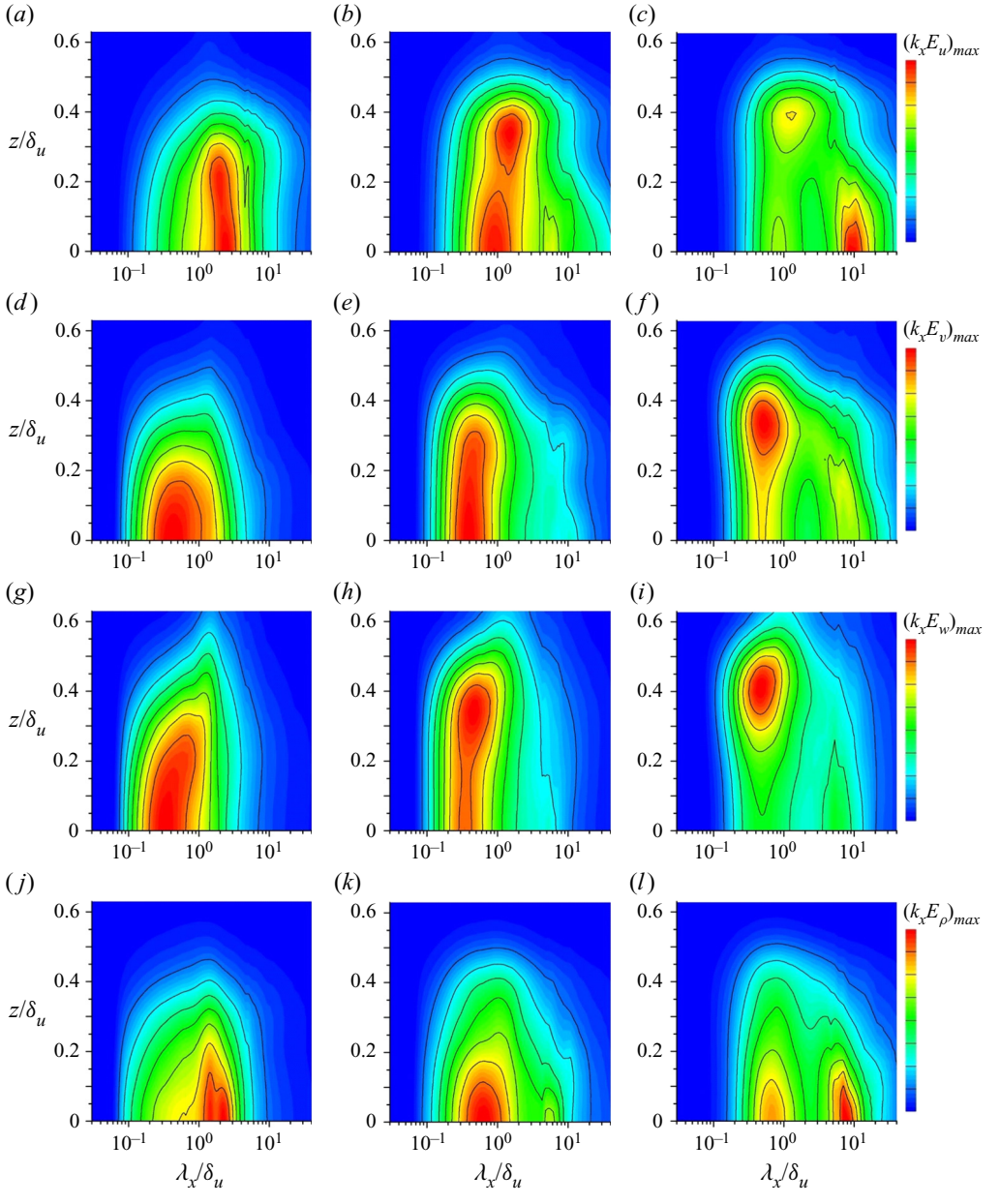


Figure 8. Premultiplied energy spectra of velocity and density, k_xE_α ($\alpha = u, v, w$ or ρ) in run 2 ($Re = 2000$, $Ri = 0.06$), plotted against the streamwise wavelength $\lambda_x = 2\pi/k_x$ and the vertical location z: (*a*,*d*,*g*,*j*) $t = 140$; (*b*,*e*,*h*,*k*) $t = 240$; (*c*,*f*,*i*,*l*) $t = 320$. (*a–c*) Streamwise velocity E_u; (*d–f*) spanwise velocity E_v; (*g–i*) vertical velocity E_w; (*j–l*) density E_ρ. The colour contours are normalized by the peak values at specific times.

stratification (Balaras, Piomelli & Wallace 2001). The peak wavelength at $Ri = 0$ and 0.02 is about $\lambda_x/\delta_u = 2$–3, which is much smaller than the size of ELSS. The ELSS corresponding to the spectral peak at $\lambda_x/\delta_u \approx 10^1$ appear only at moderately large Ri. This peak at $\lambda_x/\delta_u \approx 10^1$ appears earlier at $Ri = 0.1$ than at $Ri = 0.06$. Thus, the ELSS develop faster for higher Ri.

https://doi.org/10.1017/jfm.2021.773 Published online by Cambridge University Press

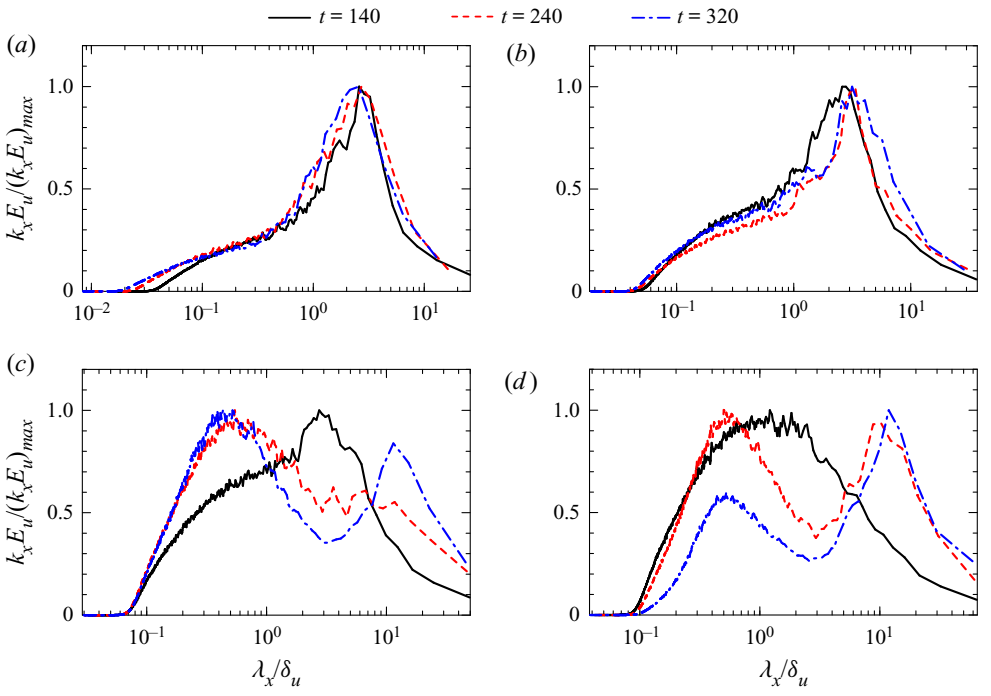


Figure 9. Energy spectra of streamwise velocity at $z = 0$ at $t = 140$, 240 and 320 in runs 3–6 ($Re = 40\,000$): (*a*) $Ri = 0$ (run 3); (*b*) $Ri = 0.02$ (run 4); (*c*) $Ri = 0.06$ (run 5); (*d*) $Ri = 0.1$ (run 6). For comparison of the spectra at different t, k_xE_u is normalized by its maximum value $[k_xE_u]_{max}$ at each time instance.

3.4. *Characteristics of large-scale velocity and density fluctuations*

The scale dependence of turbulent statistics is investigated with the energy spectra in run 2. The characteristic length scales of LSM and ELSS are estimated with the spectral peaks. Figure 10(*a*) shows the turbulent kinetic energy spectrum $E_k = (E_u + E_v + E_w)/2$ and density spectrum E_ρ at $t = 260$ on the centreline, where two peaks can be identified for both spectra. Here, the short peak-wavelength of E_ρ is denoted by $\Lambda_{S\rho}$ while the long peak-wavelength is denoted by $\Lambda_{L\rho}$. Similarly, Λ_{Sk} and Λ_{Lk} represent the short and long peak-wavelengths of E_k, respectively. The premultiplied spectra at $z = 0$ are plotted on the discrete coordinate of λ_x, where one can find the peaks in E_k and E_ρ. A third-order polynomial curve fitting with five discrete points centred at the peak of E_k or E_ρ is applied to determine the peak wavelength from the fitted curve. These peak wavelengths are the characteristic length scales of LSM and ELSS. The spectra before $t = 220$ have only a single peak at $z = 0$ and the ELSS have not formed yet. Figure 10(*b*) shows temporal variations of the peak wavelengths obtained at $z = 0$ after $t = 220$. Here, these wavelengths are normalized by δ_u, which hardly increases with time for $t \geqslant 220$ as shown in figure 5(*b*). The short peak-wavelength weakly depends on time: $\Lambda_{S\rho}$ and Λ_{Sk} stay between $0.5\delta_u$ and $0.7\delta_u$. On the other hand, the long peak-wavelengths increase with time approximately from $5\delta_u$ to $9\delta_u$. Therefore, the length scale of LSM hardly grows with time while the length of ELSS monotonically increases. The increase of Λ_{Lk} and $\Lambda_{L\rho}$ can be caused by the deformation due to mean shear. In the stratified shear layer a time scale of turbulence increases as the turbulence decays, while a time scale of the mean shear $\sim U_0/\delta_u$ is almost independent of time because δ_u hardly changes with time once the stably stratified turbulent shear layer has fully developed. Therefore, the

https://doi.org/10.1017/jfm.2021.773 Published online by Cambridge University Press

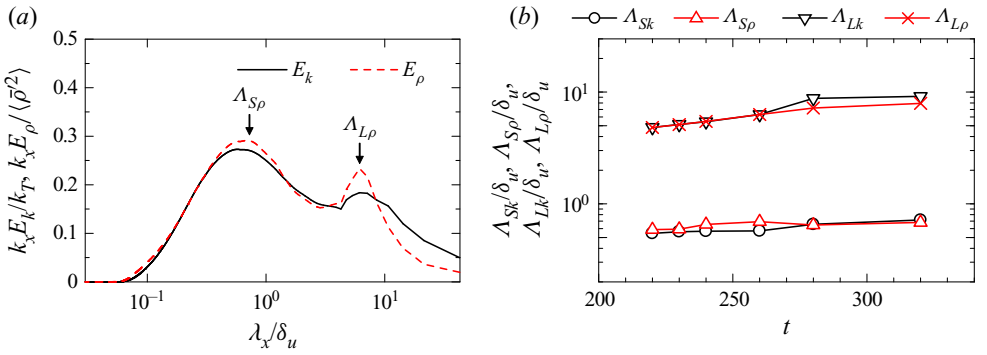


Figure 10. (*a*) Energy spectra of turbulent kinetic energy (E_k) and density (E_ρ) at $t = 260$ with the definition of short and long peak-wavelengths. The spectra multiplied by k_x are normalized by turbulent kinetic energy $k_T = (\langle\bar{u}'^2\rangle + \langle\bar{v}'^2\rangle + \langle\bar{w}'^2\rangle)/2$ or density variance $\langle\bar{\rho}'^2\rangle$. (*b*) Temporal evolution of short and long peak-wavelengths in E_k and E_ρ. These results are taken at the centre of the shear layer in run 2.

turbulence time scale becomes much longer than the shear time scale at late time. In the stably stratified shear layer investigated in this study, the integral shear parameter defined as a turbulence-to-shear time scale ratio exceeds 15 (Watanabe *et al.* 2019*a*), which is larger than typical values of 3–6 in non-stratified turbulent free shear flows (Pope 2000). In general, turbulence with larger scales evolves more slowly. Therefore, the turbulent motions, especially at scales of the ELSS, evolve much more slowly than the shear time scale, and its evolution is possibly approximated by rapid distortion theory (Savill 1987). The theory predicts that the longitudinal integral length scale in the mean flow direction monotonically increases with time in turbulence with a simple shear (Lee, Kim & Moin 1990). This behaviour is consistent with the growth of Λ_{Lk} and $\Lambda_{L\rho}$ found in figure 10(*b*).

The degree of anisotropy of the Reynolds stress tensor $R_{ij} = \langle\bar{u}_i'\bar{u}_j'\rangle$ is evaluated with the normalized anisotropy tensor defined as

$$b_{ij} = \frac{R_{ij}}{R_{kk}} - \frac{1}{3}\delta_{ij}. \tag{3.4}$$

The state of anisotropy of R_{ij} is often expressed by the Lumley triangle, which is defined with $\eta_b = (b_{ij}b_{ji}/6)^{1/2}$ and $\xi_b = (b_{ij}b_{jk}b_{ki}/6)^{1/3}$ (Pope 2000). The isotropic Reynolds stress has $(\xi_b, \eta_b) = (0, 0)$. Although the Lumley triangle was also investigated in DNS of stratified shear layers (Smyth & Moum 2000*a*; Wingstedt *et al.* 2015), small computational domains used in previous DNS did not allow the growth of ELSS. However, the spectral energy density for ELSS is not negligible in figure 8, and the ELSS might have significant influences on the anisotropy of Reynolds stress. The Lumley triangle is often used for turbulence modelling but is used as a diagnostic tool for the isotropy of Reynolds stress in this study. Because b_{ij} is defined with R_{ij} normalized by R_{kk}, it is useful to compare (ξ_b, η_b) among different flows even if these flows have different magnitudes of the turbulent kinetic energy. For example, Gargett & Wells (2007) provided the discussion on η_b and ξ_b in observations of ocean turbulence by comparing them with canonical turbulent flows, such as turbulent boundary layers.

Figure 11(*a*) shows variations of (ξ_b, η_b) from $z = 0$ to $0.5\delta_u$ at $t = 140$ and 320. The LES results (run 2) are compared with the results obtained at different heights of a turbulent boundary layer (Watanabe *et al.* 2019*b*) and at the centre of a non-stratified, fully developed turbulent mixing layer (Takamure *et al.* 2018). Here, the vertical location in the turbulent boundary layer, y, is normalized by the viscous length $\delta_\nu = \nu/u_\tau$ defined

https://doi.org/10.1017/jfm.2021.773 Published online by Cambridge University Press

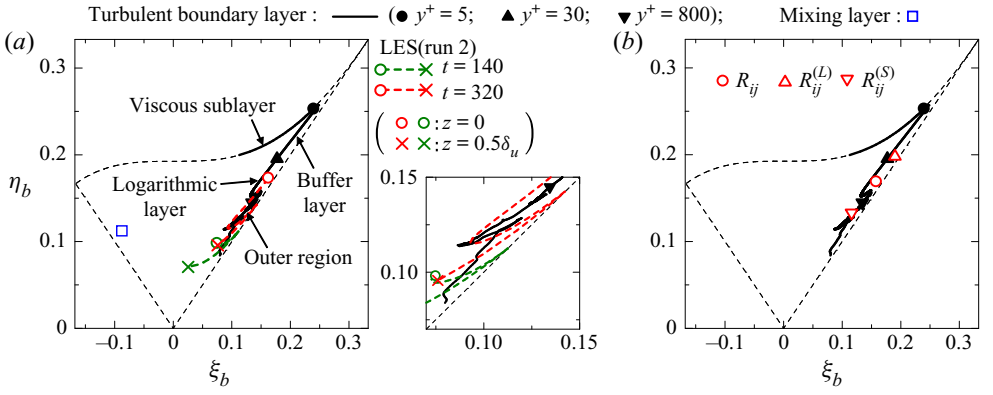


Figure 11. (*a*) Variation of ξ_b and η_b between $z = 0$ and $0.5\delta_u$ at $t = 140$ and 320 in run 2. An enlarged figure is also shown for clarity. (*b*) Plots of ξ_b and η_b associated with large and small peak-wavelengths of the turbulent kinetic energy spectrum at $z = 0$ and $t = 320$ in run 2. Three thin broken lines correspond to an axisymmetric state with one large eigenvalue, $\eta_b = \xi_b$, or one small eigenvalue, $\eta_b = -\xi_b$, and a two-dimensional state $\eta_b = (1/27 + 2\xi_b^3)^{1/2}$. Figures also include ξ_b and η_b obtained in the turbulent boundary layer at the momentum thickness Reynolds number of $Re_\theta = 13\,000$ in Watanabe *et al.* (2019*b*) and at the centre of the non-stratified, fully developed turbulent mixing layer (Takamure *et al.* 2018).

with the friction velocity $u_\tau = \sqrt{\tau/\rho}$ (τ: wall shear stress) as $y^+ = y/\delta_v$. Three locations, $y^+ = 5$, 30 and 800, represent the approximate locations that separate the viscous sublayer ($y^+ \lesssim 5$), the buffer layer ($5 \lesssim y^+ \lesssim 30$), the logarithmic layer ($30 \lesssim y^+ \lesssim 800$) and the outer region ($y^+ \gtrsim 800$). At $t = 140$, the centre of the stably stratified shear layer has $(\xi_b, \eta_b) \approx (0.08, 0.1)$ (a green circle in figure 11*a*), which is close to the outer region of the turbulent boundary layer. At $t = 320$, both ξ_b and η_b become large compared with early time. Here, the centre of the shear layer has $(\xi_b, \eta_b) = (0.16, 0.17)$ (a red circle in figure 11*a*), and the Reynolds stress is more anisotropic than at the early time. In addition, $(\xi_b, \eta_b) \approx (0.16, 0.17)$ is within the logarithmic layer in case of the turbulent boundary layer. On the other hand, the region away from the centreline still attains (ξ_b, η_b) close to the outer region of the turbulent boundary layer.

The flow has two characteristic energy-containing length scales represented by Λ_{Sk} and Λ_{Lk}. We introduce k_{min}, which represents the wavenumber corresponding to the minimum value of $k_x E_k$ at $z = 0$ between the two peaks at Λ_{Sk} and Λ_{Lk} (see figure 10*a*). The contributions to the Reynolds stress from fluctuations associated with Λ_{Sk} (LSM) and Λ_{Lk} (ELSS) are respectively evaluated by integrating a corresponding cospectrum as

$$R_{ij}^{(S)} = \int_{k_{min}}^{\infty} \mathrm{Re}[\langle \widehat{\tilde{u}_i'} \widehat{\tilde{u}_j'}^* \rangle] \, \mathrm{d}k_x, \quad R_{ij}^{(L)} = \int_0^{k_{min}} \mathrm{Re}[\langle \widehat{\tilde{u}_i'} \widehat{\tilde{u}_j'}^* \rangle] \, \mathrm{d}k_x. \tag{3.5a,b}$$

The anisotropy of velocity fluctuations associated with the LSM and ELSS is evaluated with η_b and ξ_b calculated separately from $R_{ij}^{(S)}$ and $R_{ij}^{(L)}$. Figure 11(*b*) compares η_b and ξ_b obtained from R_{ij}, $R_{ij}^{(S)}$ and $R_{ij}^{(L)}$ at $z = 0$ and $t = 320$. For fluctuations associated with the large peak-wavelength, $(\eta_b, \xi_b) \approx (0.2, 0.2)$ is obtained from $R_{ij}^{(L)}$. The turbulent boundary layer also has $(\eta_b, \xi_b) \approx (0.2, 0.2)$ between the buffer layer and the logarithmic layer, and the anisotropy of the Reynolds stress for Λ_{Lk} (ELSS) is similar to the near-wall region. However, η_b and ξ_b obtained from $R_{ij}^{(S)}$ are close to the values in the outer region. Therefore, the highly anisotropic Reynolds stress R_{ij} near the centre of the shear layer is

https://doi.org/10.1017/jfm.2021.773 Published online by Cambridge University Press

caused by the ELSS with an approximate length of Λ_{Lk}. In figure 11(a), (η_b, ξ_b) near the edge of the shear layer at $t = 320$ (a red cross in figure 11a) are still close to the values in the outer region of the turbulent boundary layer. This is explained by the absence of the ELSS near the edge of the stably stratified shear layer since the long-wavelength peak at $\lambda_x \approx \Lambda_{Lk}$ in the energy spectra does not exist at large z in figure 8(c,f,i).

A fractional contribution to the total Reynolds stress from $R_{ij}^{(L)}$ and $R_{ij}^{(S)}$ can be defined as $F_S = R_{ij}^{(S)}/R_{ij}$ and $F_L = R_{ij}^{(L)}/R_{ij}$ for each component of i and j. Similarly, F_S and F_L for density variance $\langle \bar{\rho}'^2 \rangle$ and vertical density flux $\langle \bar{\rho}' \bar{w}' \rangle$ can be defined with the integral of the corresponding spectrum and cospectrum. Figure 12(a) shows temporal variations of F_S and F_L at $z = 0$ for velocity and density variances. For all components, F_S decreases and F_L increases with time, and the contribution from the ELSS relatively becomes more important with time for velocity and density fluctuations. Figure 12(b) shows F_S and F_L obtained for the vertical turbulent fluxes of u and ρ. Unlike velocity and density variances, F_L stays around 0 even at late time, and the LSM with scales close to Λ_{Sk} dominate the vertical transfer of momentum and density. The Reynolds stress and the vertical fluxes become small at late time, and F_S and F_L only provide the relative contribution at a given time. Therefore, large F_L does not mean that the ELSS have a dominant contribution to the energetic property over the shear layer development. Figure 12(c) plots $R_{ij}^{(L)}$ and $R_{ij}^{(S)}$ for $(i, j) = (1, 1)$ and $(1, 3)$. Although $R_{11}^{(S)}$ decays with time, $R_{11}^{(L)} \approx 1$ slowly varies and the velocity fluctuations of the ELSS hardly decay. Similar results are obtained for R_{22} and R_{33} (not shown here). On the other hand, $R_{13}^{(L)}$ is close to 0 while $R_{13}^{(S)}$ also decreases to 0 with time. Thus, the ELSS hardly contribute to the vertical transport of momentum. Large scatters are found for F_L and F_S at late time in figure 12(b). This is caused by small $\langle \bar{u}' \bar{w}' \rangle$ and $\langle \bar{\rho}' \bar{w}' \rangle$, which are the denominators of F_S and F_L. Figure 12(a,b) confirm that the ELSS carry an important fraction of the turbulent kinetic energy while the vertical transport of momentum due to the ELSS is not significant. This is due to the weak correlation between u and w. In turbulent shear flows the decay of turbulent kinetic energy is caused by the viscous dissipation while the destruction of the Reynolds stress $\langle u'w' \rangle$ is caused by the pressure–strain correlation (Pope 2000). The viscous dissipation is active at small scales. However, the destruction of the Reynolds stress actively occurs at larger scales than the viscous dissipation (Takahashi *et al.* 2019). The different length scales of the decay process between the turbulent kinetic energy and the Reynolds stress is a possible reason for the weak vertical momentum transport by the ELSS with large turbulent kinetic energy.

For the turbulent kinetic energy dissipation rate, F_S and F_L are obtained by integrating $\hat{\varepsilon}^{(k)} = \hat{\varepsilon}_G^{(u)} + \hat{\varepsilon}_G^{(v)} + \hat{\varepsilon}_G^{(w)} + \hat{\varepsilon}_S^{(u)} + \hat{\varepsilon}_S^{(v)} + \hat{\varepsilon}_S^{(w)}$, i.e.

$$F_S = \frac{\displaystyle\int_{k_{min}}^{\infty} \hat{\varepsilon}^{(k)}\, \mathrm{d}k_x}{\displaystyle\int_0^{\infty} \hat{\varepsilon}^{(k)}\, \mathrm{d}k_x}, \quad F_L = = \frac{\displaystyle\int_0^{k_{min}} \hat{\varepsilon}^{(k)}\, \mathrm{d}k_x}{\displaystyle\int_0^{\infty} \hat{\varepsilon}^{(k)}\, \mathrm{d}k_x}. \tag{3.6a,b}$$

Similarly, F_S and F_L for the dissipation rate of density variance are defined with the integrals of the dissipation term $\hat{\varepsilon}^{(\rho)} = \hat{\varepsilon}_G^{(\rho)} + \hat{\varepsilon}_S^{(\rho)}$. Figure 12 shows F_S and F_L for $\hat{\varepsilon}^{(k)}$ and $\hat{\varepsilon}^{(\rho)}$. Even at late time, F_L is close to 0, and the ELSS have only a small contribution to the dissipation. It should be noted that $F_S \approx 1$ does not mean that the LSM causes the

https://doi.org/10.1017/jfm.2021.773 Published online by Cambridge University Press

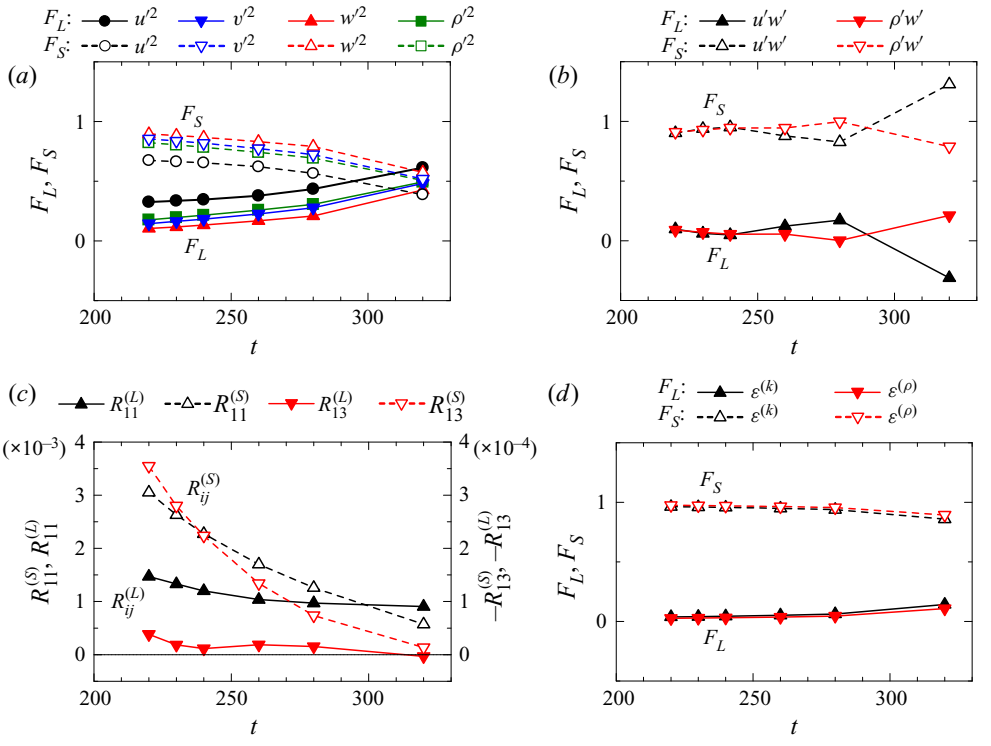


Figure 12. Fractional contributions of fluctuations associated with long and short peak-wavelengths (F_L and F_S) of E_k to (*a*) velocity and density variances, (*b*) vertical turbulent fluxes of streamwise velocity and density. (*c*) Reynolds stress associated with long and short peak-wavelengths, $R_{ij}^{(L)}$ and $R_{ij}^{(S)}$, for $(i, j) = (1, 1)$ and $(1, 3)$. Figure (*d*) shows F_L and F_S for the dissipation rates of turbulent kinetic energy and density variance. These results are taken at $z = 0$ in run 2.

dissipation because F_S includes the contribution from velocity and density fluctuations at smaller scales than the LSM.

3.5. *Energy budget in wavenumber space*

The spectral budget equations are analysed to investigate temporal evolutions of the spectra. Here, each term in the budget equations is premultiplied by k_x, and is plotted as a function of λ_x/δ_u at a given location of z/δ_u, where a logarithmic scale is used for λ_x. The LES results (run 2) are presented for $z/\delta_u = 0$ and 0.4 and for $t = 140$ and 240 because the spectral shapes are very different between these heights and times. The diffusive terms $\hat{D}^{(u_\alpha)}$ and $\hat{D}^{(\rho)}$ in (2.14) and (2.16) are about 10^1–10^2 times smaller than other spatial transport terms, and these terms are not shown in this paper.

3.5.1. *Spectral energy budget at early time*

Figure 13(*a–f*) presents the spectral energy budget (2.14) at $t = 140$ for E_u, E_v and E_w. The left and right columns of the figure show the results at $z = 0$ and $0.4\delta_u$, respectively. In figure 13(*a*,*b*) the production term $\hat{P}^{(u)}$ is mostly positive for a wide range of λ_x. At both vertical locations, $\hat{P}^{(u)}$ peaks at $\lambda_x/\delta_u \approx 1$, and the energy production is the most active for the length scale close to δ_u, i.e. the length scale of the LSM.

https://doi.org/10.1017/jfm.2021.773 Published online by Cambridge University Press

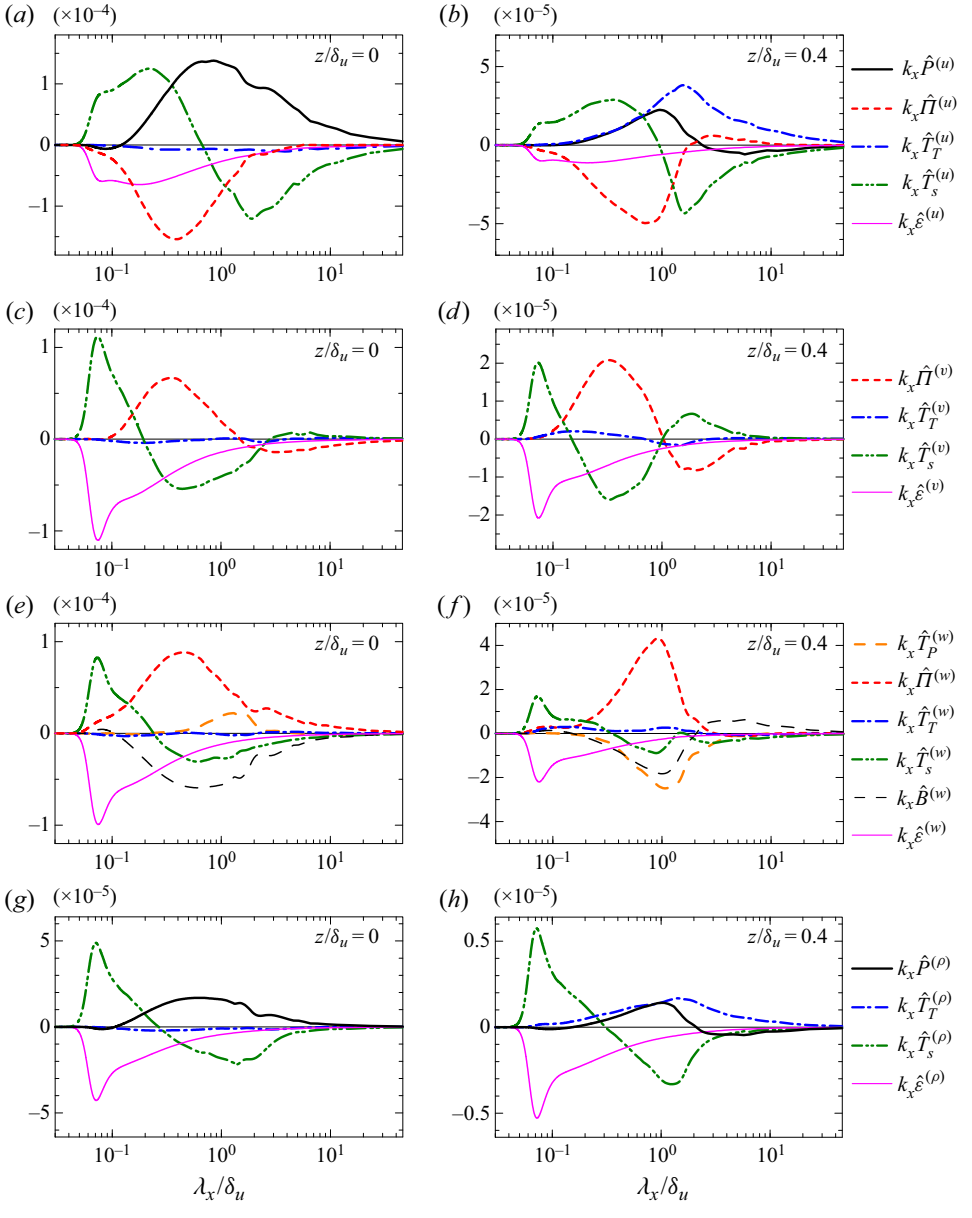


Figure 13. Spectral energy budgets of (*a*,*b*) streamwise velocity, (*c*,*d*) spanwise velocity, (*e*,*f*) vertical velocity and (*g*,*h*) density at $t = 140$ in run 2. Results are shown for (*a*,*c*,*e*,*g*) $z = 0$ and (*b*,*d*,*f*,*h*) $z = 0.4\delta_u$. Each term in the energy budget equations is plotted against the streamwise wavelength $\lambda_x = 2\pi/k_x$.

This is consistent with canonical turbulent free shear flows, where the energy production occurs at large scales, which can be characterized by the width of the flow in the transverse (cross-flow) direction. Positive production can also be seen for very large scales $\lambda_x/\delta_u \approx 10^1$ at $z = 0$, and the energy production at very large scales already occurs at the early time. This energy produced at $\lambda_x/\delta_u \approx 10^1$ is removed by the interscale transport term $\hat{T}_S^{(u)}$.

https://doi.org/10.1017/jfm.2021.773 Published online by Cambridge University Press

In figure 13(*a*,*b*) the pressure–strain correlation $\hat{\Pi}^{(u)}$ is mostly negative, and large negative $\hat{\Pi}^{(u)}$ appears for the range of λ_x with large positive $\hat{P}^{(u)}$. In figure 13(*c*–*f*), $\hat{\Pi}^{(v)}$ and $\hat{\Pi}^{(w)}$ tend to be positive for the wavelength with negative $\hat{\Pi}^{(u)}$. The energy of $\bar{u}'$, increased by the production, is partially redistributed to those of $\bar{v}'$ and $\bar{w}'$ at large scales close to $\lambda_x \approx \delta_u$. In figure 13(*c*), $\hat{\Pi}^{(v)}$ is negative for $\lambda_x/\delta_u \gtrsim 2$, for which $\hat{\Pi}^{(w)}$ in figure 13(*e*) is positive, and the energy is redistributed from $\bar{v}'$ mainly to $\bar{w}'$. The wavelength of this energy redistribution is larger than the peak wavelength of the positive energy production for E_u. Interestingly, similar behaviour of the pressure–strain correlation was reported in channel flows (Lee & Moser 2019): the energy of the streamwise velocity is redistributed to the vertical (wall-normal) and spanwise velocity components at large scales, while for even larger scales, the energy of the spanwise velocity is redistributed to that of the vertical velocity.

The dissipation terms $\varepsilon^{(u_\alpha)} = \varepsilon_G^{(u_\alpha)} + \varepsilon_S^{(u_\alpha)}$ have a negative peak at small scales as expected from the scale dependence of the energy dissipation in turbulence. The turbulent diffusion terms $\hat{T}_T^{(u_\alpha)}$ are relatively small compared with other important terms at $z = 0$ in figure 13(*a*,*c*,*e*). However, $\hat{T}_T^{(u)}$ at $z/\delta_u = 0.4$ is the main source of the energy growth at large scales in figure 13(*b*). Pham & Sarkar (2010) also found that the turbulent kinetic energy is transferred outward in the stably stratified shear layer. On the other hand, $\hat{T}_T^{(v)}$ and $\hat{T}_T^{(w)}$ are smaller than other important terms even at $z/\delta_u = 0.4$, where the pressure–strain correlation is the source of the energy.

The interscale transport term $\hat{T}_S^{(u)}$ in figure 13(*a*,*b*) is positive for $\lambda_x/\delta_u \lesssim 0.8$ and is negative for larger scales. Similarly, positive and negative $\hat{T}_S^{(w)}$ in figure 13(*e*,*f*) can be found for small and large scales, respectively. Therefore, a forward energy transfer from large to small scales occurs for the energy of $\bar{u}'$ and $\bar{w}'$. However, $\hat{T}_S^{(v)}$ in figure 13(*c*,*d*) exhibits negative values for $0.2 \lesssim \lambda_x/\delta_u \lesssim 2$, which are surrounded by positive values for larger and smaller scales. This profile indicates that the energy at scales of $0.2 \lesssim \lambda_x/\delta_u \lesssim 2$ is transferred to both large and small scales. Positive $\hat{T}_S^{(v)}$ for $\lambda_x/\delta_u \gtrsim 2$ appears for the wavelength with negative $\hat{\Pi}^{(v)}$. Therefore, the interscale energy transfer of $\bar{v}'$ feeds the energy at large scales, which is further redistributed by the pressure–strain correlation. At $t = 140$, the Ozmidov scale is $L_O/\delta_u = 6.9 \times 10^{-2}$ at the centre of the shear layer. Turbulent motions with scales greater than the Ozmidov scale are expected to be strongly suppressed by the buoyancy (Riley & Lindborg 2008). However, $\hat{T}_S^{(u_\alpha)}$ confirms that the forward energy transfer occurs for length scales larger than the Ozmidov scale, indicating that the active interscale transport in the turbulent shear layer is possible even under the strong influence of stable stratification. It is interesting to note that the scale dependence of $\hat{T}_S^{(u_\alpha)}$ in the stably stratified shear layer is consistent with DNS results of channel flows (Lee & Moser 2019). Above the buffer layer of the channel flow, an interscale transfer from large to small scales occurs for the energy of streamwise and vertical velocities while the energy of spanwise velocity is transferred to both large and small scales.

The pressure diffusion and buoyancy flux terms appear only in the equation for E_w shown in figure 13(*e*,*f*). The pressure diffusion term for $\lambda_x/\delta_u \approx 10^0$ is positive at $z = 0$ and negative at $z/\delta_u = 0.4$, and transfers the energy toward the middle of the shear layer at large scales. The profile of the buoyancy flux is similar to the pressure–strain correlation with opposite signs, and the energy converted to w' is partially removed by the buoyancy force.

https://doi.org/10.1017/jfm.2021.773 Published online by Cambridge University Press

Figure 13(*g*,*h*) shows the spectral energy budget of density fluctuations, (2.16), at $t = 140$. Both streamwise velocity and density fluctuations are produced by the vertical gradients of $\langle u \rangle$ and $\langle \rho \rangle$, whose initial profiles are given by a hyperbolic tangent function. Therefore, the spectral energy budget is similar between E_u and E_ρ at $t = 140$.

3.5.2. *Spectral energy budget at late time*

Figure 14(*a–f*) presents the spectral energy budget at $t = 240$ for three velocity components. At $t = 240$, E_u and E_ρ have a second peak associated with the ELSS while the long-wavelength peak is forming in E_v and E_w (figure 8). For E_u, the dissipation, turbulent transport and interscale transfer terms are qualitatively similar at $t = 140$ and 240 while $\hat{P}^{(u)}$ and $\hat{\Pi}^{(u)}$ have different profiles. The production $\hat{P}^{(u)}$ at $t = 240$ has a large peak at $\lambda_x/\delta_u \approx 0.6$ at both heights. At $z = 0$, $\hat{P}^{(u)}$ has a second peak for $\lambda_x/\delta_u \approx 10$, which does not exist at $t = 140$. The energy production for $\lambda_x/\delta_u \approx 10$ does not occur at $z/\delta_u = 0.4$, where the ELSS do not appear. Negative $\hat{\Pi}^{(u)}$ appears for $0.1 \lesssim \lambda_x/\delta_u \lesssim 1$, where the production term has large positive values. As also found at early time, the energy produced by the mean velocity gradient is redistributed to other velocity components for this wavelength range. However, this energy redistribution does not occur at $\lambda_x/\delta_u \approx 10$, where the energy production is active. Comparisons of all terms shown in figure 14(*a*) imply that the growth of the ELSS at $\lambda_x/\delta_x \approx 10^1$ is mainly caused by the energy production at very large scales.

The most terms for the budget of E_v are qualitatively similar between $t = 140$ and 240. However, negative $\hat{\Pi}^{(v)}$ at $\lambda_x/\delta_u \gtrsim 5$ found at $t = 140$ is not observed at $t = 240$, and $\hat{\Pi}^{(v)}$ does not cause the decay of E_v at very large scales. For E_w, time dependence is significant for $\hat{T}_P^{(w)}$ and $\hat{\Pi}^{(w)}$. The pressure diffusion $\hat{T}_P^{(w)}$ at $t = 240$ is positive at $\lambda_x/\delta_u \approx 10$ while $\hat{\Pi}^{(w)}$ is close to 0 for $\lambda_x/\delta_u \gtrsim 2$ at $t = 240$. Thus, the pressure effect contributes to the energy growth at very large scales at $z = 0$.

Figure 14(*g*,*h*) shows the budget of E_ρ at $t = 240$. Difference between $t = 140$ and 240 is similar for E_u and E_ρ. A long-wavelength peak of the production term appears at $\lambda_x/\delta_u \approx 10$ at $t = 240$ in figure 14(*g*), and the production at the very large scales generates the density fluctuations of ELSS.

One of the noteworthy features for the budgets of E_u and E_ρ is small negative production at small scales of $\lambda_x/\delta_u \approx 0.1$ in figure 14(*a*,*b*,*g*,*h*). Even at $t = 140$, the production terms have small negative values for $\lambda_x/\delta_u \approx 0.1$ in figure 13(*a*). These negative values of the production terms are also found in DNS (not shown here) and are not artificially caused by the implicit SGS model. The negative production requires $Re[\langle \widehat{\tilde{u}}'^* \widehat{\tilde{w}}' \rangle] > 0$ and $Re[\langle \widehat{\tilde{\rho}}^* \widehat{\tilde{w}}' \rangle] < 0$. These cospectra represent the spectral density of the turbulent fluxes. The signs of the cospectra corresponding to the negative production are associated with the counter-gradient transports of streamwise momentum and density. This is contrary to the spectral analysis of Reynolds stress of a fully developed turbulent mixing layer without density stratification, where the turbulent momentum transport is in the down-gradient direction for all length scales (Takamure *et al.* 2018). Interestingly, negative values of the production term of the turbulent kinetic energy spectrum were also found in channel flows (Lee & Moser 2019). Around vertical locations between the buffer layer and logarithmic layer of the channel flow, the production term has large positive values at large scales while negative production appears for slightly smaller wavelengths than the positive production. As in the stably stratified shear layer considered in this study, the negative production in the channel flow is small compared with their positive peak at large scales.

https://doi.org/10.1017/jfm.2021.773 Published online by Cambridge University Press

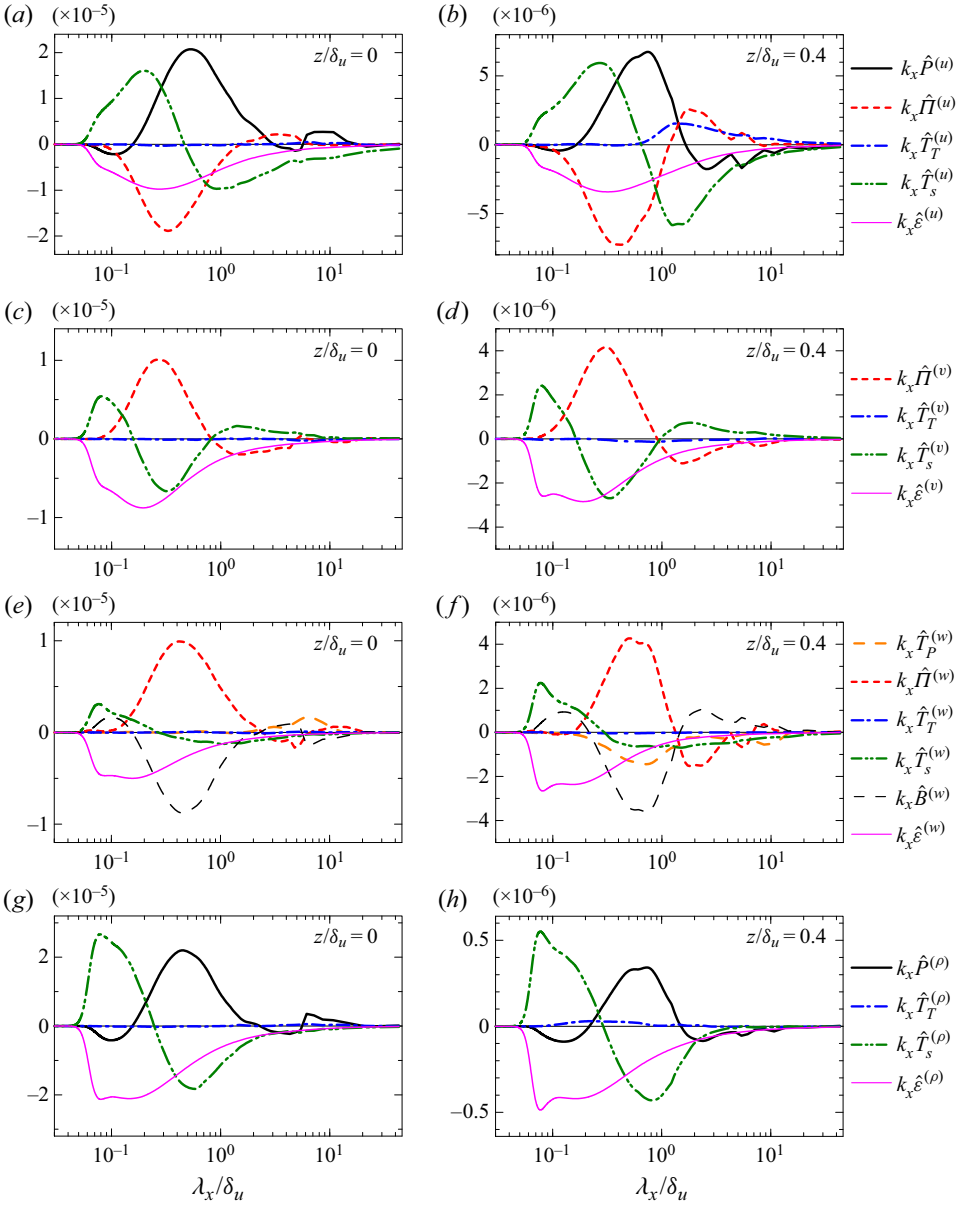


Figure 14. Same as figure 13, but at $t = 240$.

3.5.3. *Formation of double-peak energy spectra on the shear layer centreline*

From $t = 140$ to 240, the spectral shape at $z = 0$ changes from a single-peak profile to a double-peak profile. The formation of the double-peak spectrum can be clearly appreciated by $T_\alpha^{-1} \equiv (\partial E_\alpha/\partial t)/E_\alpha$, which can be interpreted as the rate (inverse of time scale) of the spectral evolution. Figure 15 shows T_α^{-1} for three velocity components and density at $t = 140$ and 240 at the centre of the shear layer. For $\lambda_x/\delta_u \lesssim 0.1$, T_α^{-1} becomes large as λ_x decreases. This is because the energy spectra become extremely small as the implicit SGS model dissipates the energy at resolved small scales. The energy spectra decay with time

https://doi.org/10.1017/jfm.2021.773 Published online by Cambridge University Press

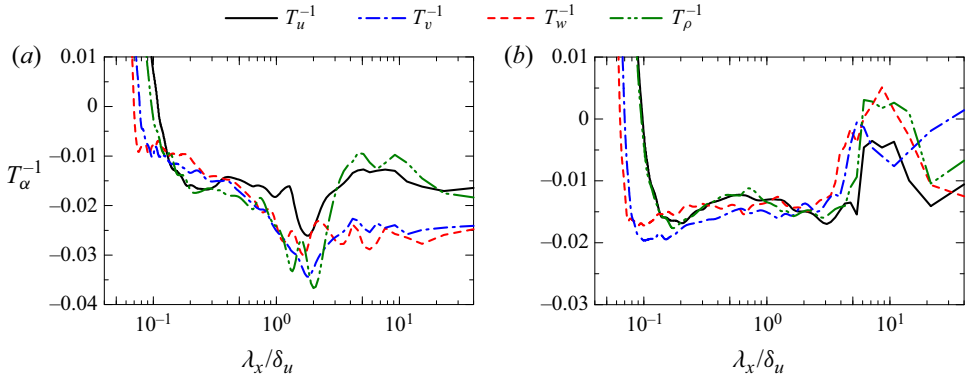


Figure 15. The rate of the change in energy spectra defined as $T_\alpha^{-1} = (\partial E_\alpha/\partial t)/E_\alpha$ for $\alpha = u, v, w$ and ρ at $z = 0$ in run 2: (*a*) $t = 140$; (*b*) $t = 240$.

as also confirmed from $T_\alpha^{-1} < 0$ for most wavelengths. At $t = 240$, the decay rate is small at $\lambda_x/\delta_u \approx 10$, which is the length scale of the ELSS. Therefore, the velocity fluctuations of the ELSS decay more slowly than those of the LSM. The scale dependence of T_α^{-1} suggests that the spectrum with a single peak rapidly decays with time except for very large scales, and eventually the double-peak spectrum is formed once the spectrum decays sufficiently except for $\lambda_x/\delta_u \approx 10$. At $t = 140$ in figure 15(*a*), the slow decay of energy spectra at $\lambda_x/\delta_u \approx 10$ is found only for E_u and E_ρ. Thus, the decay of E_v and E_w is faster at larger scales. Consistently, the formation of the double-peak spectra occurs at earlier time for E_u and E_ρ than for E_v and E_w in figure 8.

Figure 16(*a*) shows the production term $k_x\hat{P}^{(u)}$ normalized by its maximum value $[k_x\hat{P}^{(u)}]_{max}$ at $z = 0$ at four time instances. At $t = 140$, the energy is produced for a wide range of length scales. However, the shape of $k_x\hat{P}^{(u)}$ changes from $t = 140$ to 230, and the production term at late time has two peaks corresponding to the peaks in E_u. The energy production at $\lambda_x/\delta_u \approx 10$ becomes more important at late time. The production is almost zero or can be negative for $\lambda_x/\delta_u \approx 6$. This negligible production is consistent with E_u in figure 8(*c*), where E_u is locally small for the wavelength with small $k_x\hat{P}^{(u)}$. The wavelength of positive production corresponding to the long-wavelength peak is shifted to larger scales with time as also expected from the increase of the long peak-wavelength in figure 10(*b*). Figure 16(*b*) shows the sum of the pressure terms, $\hat{P}_r^{(w)} = \hat{T}_P^{(w)} + \hat{\Pi}^{(w)}$, at $z = 0$, where $\hat{P}_r^{(w)}$ is premultiplied by k_x and normalized by the maximum value of $k_x\hat{P}_r^{(w)}$. The pressure terms of E_w play a similar role to the production term of E_u: the energy growth at $\lambda_x/\delta_u \approx 0.5$ and 10 is caused by the pressure effects for E_w and by the production for E_u. The pressure effects are responsible for the change in the shape of E_w. Similar time dependence was found for the production term of density (not shown here). For E_v, we cannot identify a single term that is responsible for the formation of the double-peak spectrum. The growth of E_v at large λ_x is dominated by the interscale energy transfer $\hat{T}_S^{(v)}$ in figure 14(*c*), where the energy transfer from small to large scales occurs. The decrease of E_v by the pressure–strain correlation for $\lambda_x/\delta_u \approx 10$ occurs at $t = 140$ but not at $t = 240$ as shown in figures 13(*c*) and 14(*c*). The balance of these terms causes the slow decay rate of very large-scale fluctuations in figure 15(*b*).

https://doi.org/10.1017/jfm.2021.773 Published online by Cambridge University Press

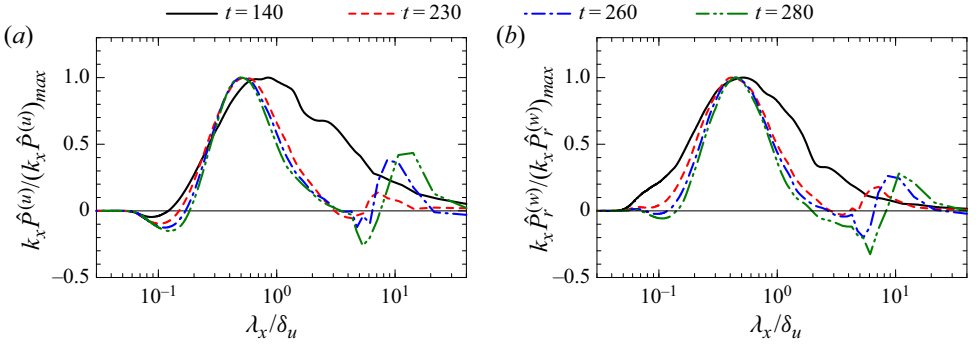


Figure 16. Temporal variations of (*a*) production term $\hat{P}^{(u)}$ of E_u and (*b*) pressure term $\hat{P}_r^{(w)} = \hat{\Pi}^{(w)} + \hat{T}_P^{(w)}$ of E_w on the centreline ($z = 0$) in run 2. The terms $k_x\hat{P}^{(u)}$ and $k_x\hat{P}_r^{(w)}$ are normalized by their maximum values, $[k_x\hat{P}^{(u)}]_{max}$ and $[k_x\hat{P}_r^{(w)}]_{max}$.

3.6. *Scaling of energy spectrum and structure function*

Another interesting feature in the energy spectra in figure 8 is that the premultiplied spectrum at a fixed height is roughly constant for a certain wavenumber range at $t = 320$, implying a k_x^{-1} power law. For example, k_xE_u in figure 8(*c*) weakly depends on the wavenumber for $2 \lesssim \lambda_x/\delta_u \lesssim 4$ near the centreline, while the range with constant k_xE_u extends to smaller scales at $z/\delta_u \approx 0.25$, where large peaks at $\lambda_x/\delta_u \approx 1$ and 10 do not exist. As discussed above, some terms of the spectral energy equations have similar wavenumber dependence in the stably stratified shear layer and wall-bounded shear flows. Furthermore, turbulent structures that have been observed in the wall-bounded shear flows were also observed in the stably stratified shear layer, e.g. hairpin vortices and ELSS (Watanabe *et al.* 2019*a*). Both stable stratification and a wall cause the suppression of vertical turbulent motions, which may lead similar turbulent characteristics in these flows. Interestingly, the scaling $E_u \sim k_x^{-1}$ has also been predicted and experimentally confirmed in wall turbulence (Perry & Chong 1982; Nickels *et al.* 2005). The equivalent scaling in real space can be written with the velocity structure function, which is defined as $\langle(\Delta u)^2\rangle = \langle[\bar{u}(x + r, y, z) - \bar{u}(x, y, z)]^2\rangle$ with a separation distance r in the x direction. The scaling law of $\langle(\Delta u)^2\rangle$ corresponding to $E_u \sim k_x^{-1}$ is the logarithmic law given by $\langle(\Delta u)^2\rangle \sim \ln(r)$ (Davidson, Nickels & Krogstad 2006). The physical basis underlying these scaling laws is the existence of turbulent motions with a range of scales which are characterized by a common velocity scale. Davidson *et al.* (2006) also pointed out that the logarithmic law is more easily observed than the k_x^{-1} law because of the aliasing problem of one-dimensional spectra.

Figure 17(*a–c*) shows the structure functions of u, v and w at $t = 320$ at three vertical locations. Here, the structure functions of v and w are $\langle(\Delta v)^2\rangle = \langle[\bar{v}(x + r, y, z) - \bar{v}(x, y, z)]^2\rangle$ and $\langle(\Delta w)^2\rangle = \langle[\bar{w}(x + r, y, z) - \bar{w}(x, y, z)]^2\rangle$. Except near the edge of the shear layer ($z/\delta_u = 0.46$), the logarithmic law is valid for a certain range of large scales. The broken lines in (*a*) represent $\langle(\Delta u)^2\rangle = A + B\ln(r)$ with A and B obtained by the least square method, which is applied for $1.2 \leqslant r/\delta_u \leqslant 2.8$ at $z = 0$ and $0.4 \leqslant r/\delta_u \leqslant 2.8$ at $z/\delta_u = 0.23$. In figure 17(*b,c*) the logarithmic law is also shown with the broken lines, which are obtained with the least square method applied for $0.97 \leqslant r/\delta_u \leqslant 2.4$ at $z = 0$ and $0.81 \leqslant r/\delta_u \leqslant 1.6$ at $z/\delta_u = 0.23$. The logarithmic law holds for all velocity components. However, A and B are not universal and are different for each velocity component and vertical location. Figure 17(*d*) shows the premultiplied spectrum k_xE_u at

https://doi.org/10.1017/jfm.2021.773 Published online by Cambridge University Press

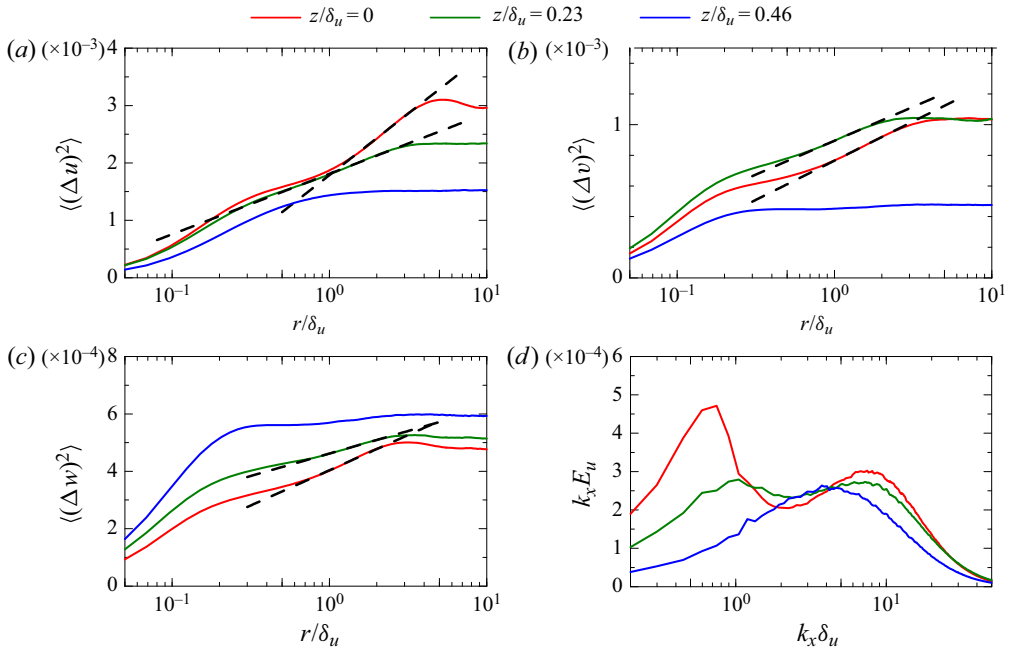


Figure 17. Structure functions of (*a*) streamwise velocity $\langle(\Delta u)^2\rangle$, (*b*) spanwise velocity $\langle(\Delta v)^2\rangle$ and (*c*) vertical velocity $\langle(\Delta w)^2\rangle$ at $t = 320$. The broken lines represent $A\ln(r/\delta_u) + B$ with A and B obtained with the least square method applied for $z = 0$ and $0.23\delta_u$. (*d*) Premultiplied energy spectrum of streamwise velocity, k_xE_u, at $t = 320$. These results are taken at $z/\delta_u = 0$, 0.23 and 0.46 in run 2.

the same locations. Although there is a range of k_x where k_xE_u weakly depends on k_x, this wavenumber range of constant k_xE_u at $z = 0$ is not as clear as the $\ln(r)$ law in figure 17(*a*), as also expected from the comparison between the k_x^{-1} and logarithmic laws in turbulent boundary layers (Davidson *et al.* 2006). Near the centre of the shear layer, $E_\alpha \sim k_x^{-1}$ tends to appear for the scales between two peaks in figure 8(*c*,*f*,*i*). In figure 8(*c*), E_u does not have large peaks at $z/\delta_u \approx 0.25$, where the logarithmic law is valid for a wide range of scales in figure 17(*a*). Therefore, the logarithmic law is clearly observed for large scales when the scales are not affected by the spectral peaks of LSM and ELSS. As the scale separation between LSM and ELSS increases with time, the $\ln(r)$ law and k^{-1} law may be more clearly observed at further later time.

3.7. *Comparison between the stably stratified shear layer and wall turbulence*

The ELSS develop at late time in the stably stratified shear layer. Similar structures, known as superstructures or very LSM, also exist in wall-bounded turbulent shear flows, e.g. channel, pipe and boundary-layer flows (Hutchins & Marusic 2007; Monty *et al.* 2009). It was also shown that a large number of hairpin vortices exist in the stably stratified shear layer, where the hairpin vortices induce velocity fluctuations at the streamwise length scale of LSM (Watanabe *et al.* 2019*a*). Thus, the stably stratified shear layer at late time resembles the wall turbulence in terms of the turbulent structures. Furthermore, the LES results presented above also confirm that some statistics are also qualitatively similar in these flows, e.g. the energy budget in wavenumber space, the anisotropy of Reynolds stress tensor and the logarithmic law of the velocity structure functions at large scales.

https://doi.org/10.1017/jfm.2021.773 Published online by Cambridge University Press

As confirmed from the energy spectra, the ELSS emerge at late time for $Re = 2000$ and 40 000 when Ri is not too small. The detailed process of turbulent transition depends on the Reynolds number and Richardson number (Mashayek & Peltier 2012; Thorpe 2012). Therefore, the transition process is not directly related to the formation of ELSS. This is also supported by the flow visualization in figure 4: the velocity fluctuations of the ELSS are hardly correlated with the velocity profiles associated with the Kelvin–Helmholtz instability and the initial velocity fluctuations. The spectral energy budget in § 3.5 also confirms that the flow dynamics is similar between the stably stratified shear layer and channel flow. Therefore, it is reasonable to assume that the ELSS in these flows are generated by the same mechanism. However, there is also a possibility that the ELSS is generated and sustained by long internal gravity waves, which may dominate the velocity fluctuations at the late time. Further investigation is required to clarify the generation mechanism of the ELSS. The ELSS develop even if Re_b is larger than 100 ($Re = 40\,000$, $Ri = 0.06$). The present LES suggests that Ri or Ri_g is an important parameter in the development of the ELSS because the ELSS are not observed for $(Re, Ri) = (40\,000, 0.02)$, for which Ri_g in table 2 is below the critical Richardson number 1/4 (Miles 1961). On the other hand, the ELSS are observed for $Ri = 0.06$ and 0.1, for which Ri_g exceeds the critical value. At $Ri = 0$ and 0.02, δ_u grows with time even at late time in figure 7(*a*). However, δ_u hardly increases with time for $Ri = 0.06$ and 0.1 after the turbulent transition, and the vertical length scale of the flow does not vary with time. In wall turbulence the largest vertical length scale of turbulence at a given height is also fixed as the distance from the wall. The confinement of the growth of the vertical length scale is possibly important in the formation of the ELSS in these flows.

Negative production of E_u and E_ρ at small scales is observed in figure 14(*a*,*b*,*g*,*h*). As explained above, the negative production is due to the counter-gradient transport of streamwise momentum and density. Previous studies on stratified turbulence also observed the counter-gradient transport regardless of the presence of mean shear (Lienhard & van Atta 1990; Holt, Koseff & Ferziger 1992; Komori & Nagata 1996). However, the physical mechanism of the counter-gradient transport in stratified turbulence may depend on the mean shear as discussed in Gerz & Schumann (1996). They explained the counter-gradient transport at small scales in stratified turbulence with mean shear based on the collision of fluid parcels which are vertically transferred by inclined hairpin vortices generated by the mean shear. Indeed, a large number of hairpin vortices develop in the stably stratified shear layer (Watanabe *et al.* 2019*a*). Gerz & Schumann (1996) also suggested that the same mechanism can also cause the counter-gradient transport of momentum in wall-bounded shear flows, where the hairpin vortices have also been found in numerous studies (e.g. Wu & Moin 2009). The wavenumber dependence of the production terms of E_u and E_ρ is also qualitatively similar between the middle of the shear layer (figure 14*a*) and the buffer and logarithmic layers of channel flows (Lee & Moser 2019). Thus, the mechanism of the counter-gradient momentum transport proposed by Gerz & Schumann (1996) seems to be valid in these flows.

The integral shear parameter $S^* = Sq^2/\varepsilon^{(k)}$ ($q^2 = \langle u_i' u_i' \rangle$) represents the time scale ratio of the eddy turnover time $q^2/\varepsilon^{(k)}$ to the mean-shear time scale $S^{-1} = \langle \partial u/\partial z \rangle^{-1}$. The evolution of turbulence is strongly influenced by the mean shear when S^* is much larger than 1. Non-stratified turbulent free shear flows have $S^* \approx 3$–6 (Pope 2000) while the stably stratified turbulent shear layer at $z = 0$ has $S^* \geqslant 10$, which continuously increases with time. At $(Re, Ri) = (2000, 0.06)$, S^* reaches about 30 at $t = 320$ (Watanabe *et al.* 2019*a*) and $S^* \approx 30$ is as large as in the buffer layer of channel flows (Jiménez 2013). The counter-gradient transport by the mechanism proposed in Gerz & Schumann (1996)

https://doi.org/10.1017/jfm.2021.773 Published online by Cambridge University Press

is simply due to the strong influence of mean shear and is not directly related to the stable stratification. Therefore, the counter-gradient momentum transport at small scales occurs in homogeneous shear flow with $S^* \approx 30$ even without stable stratification (Iida & Nagano 2007), where the shape of the cospectrum of the vertical momentum-flux is qualitatively similar to $\hat{P}^{(u)}$ in figure 16(*a*) except the scales of the ELSS. The mean shear S in a temporally evolving, turbulent shear layer decreases with time in the absence of stable stratification because the shear layer thickness increases. Therefore, although the eddy turnover time $q^2/\varepsilon^{(k)}$ becomes large with time, S^* stays small and the counter-gradient transport does not occur without stable stratification (Takamure *et al.* 2018). The stable stratification suppresses the growth of the shear layer thickness. Thus, $S \sim U_0/\delta_u$ hardly varies with time while S^* increases with time because of the increase of the eddy turnover time. Therefore, the stably stratified shear layer at late time has large S^*, and the strong influence of the mean shear can result in the counter-gradient transport at small scales.

4. Conclusions

Direct numerical simulation and implicit LES were performed for a temporally evolving, stably stratified turbulent shear layer with a large computational domain that can contain ELSS. The moderate computational cost of LES enabled us to repeat the simulations with different initial velocity fluctuations and to perform ensemble averages, which are difficult in DNS because of the computational cost. The statistics calculated with ensemble averages allowed detailed quantitative investigations of statistics related to large-scale flow characteristics. The main analyses were reported for $Re = 2000$ and $Ri = 0.06$, for which the Kelvin–Helmholtz instability generates turbulence. As summarized below, some statistics reported in this paper qualitatively agree with those in channel and boundary-layer flows, indicating similar flow dynamics in the stratified shear layer and wall-bounded shear flows.

The shape of the energy spectra calculated with Fourier transform in the streamwise direction drastically changes with time: the velocity and density spectra near the centreline have a single peak in the wavenumber space at early time and double peaks at late time. Thus, the flow at late time has two energy-containing length scales. One is close to the shear layer thickness, which is a typical scale of LSM of turbulent mixing layers even without stable stratification. This energy-containing length scale exists even at early time. The other length scale is larger than the shear layer thickness and is close to the streamwise length of ELSS, which are visualized as positive and negative velocity fluctuations on horizontal planes. Large eddy simulations with $Re = 40\,000$ confirmed that the ELSS appear at $Ri = 0.06$ and 0.1 but not at $Ri = 0$ and 0.02. The streamwise length scale of LSM hardly changes with time while that of ELSS monotonically increases. The length of the ELSS reaches about 10 times the shear layer thickness. The LSM exists in the entire shear layer while the ELSS appears only near the centreline at late time. The velocity and density fluctuations of the ELSS hardly decay with time. Therefore, the contributions of the ELSS to velocity and density variances become important with time and account for about 50 % of velocity and density fluctuations at late time. However, the vertical turbulent transport of momentum and density are still dominated by the LSM. The ELSS also hardly contributes to the dissipation of velocity and density fluctuations. The Reynolds stress associated with the ELSS is highly anisotropic, with a degree of anisotropy on a Lumley triangle close to the near-wall region of a turbulent boundary layer. However, the LSM has Reynolds stress which is as anisotropic as in the outer region of the turbulent boundary layer.

https://doi.org/10.1017/jfm.2021.773 Published online by Cambridge University Press

The budget equations were evaluated for the velocity and density spectra (E_u, E_v, E_w and E_ρ). The interscale energy flux transfers the energy of streamwise velocity fluctuations u' and vertical velocity fluctuations w' from large to small scales while the energy of spanwise velocity fluctuations v' is transferred to both large and small scales. Before the ELSS has developed, the energy of v' at very large scales is converted mainly to the energy of w' by the pressure–strain correlation, where the source of this energy conversion is the interscale energy transfer of v' from small scales. The production terms of E_u and E_ρ have a peak at the scales of LSM while they become negative at slightly smaller scales than the scales with the positive production. These negative productions are related to the counter-gradient transport of streamwise momentum and density. The spectral analysis of channel flows also found similar behaviour of the production, pressure–strain correlation and interscale energy transfer terms (Lee & Moser 2019). Once the ELSS has developed, the production terms of E_u and E_ρ have two peaks near the centre of the shear layer, where the energy is produced at the wavelengths of the LSM and ELSS. Furthermore, the role of the pressure terms of E_w is similar to the production of E_u: the growth of E_w by the pressure terms occurs at the wavelengths of the LSM and ELSS. When the double-peak spectra are forming at late time, the decay of the energy spectrum at the scales of ELSS is much slower than at the small scales of LSM. This slow decay rate of the large-scale fluctuations results in the formation of the ELSS.

The scaling of the energy spectrum at large scales was also explored in comparison with wall-bounded turbulent shear flows. The present LES suggested that the logarithmic law of the velocity structure functions holds for large scales in the stably stratified shear layer. The logarithmic law for the structure function of u was observed for a wide range of the scales at vertical heights where the energy spectrum does not have large peaks of the LSM and ELSS. The corresponding scaling of the energy spectrum is the k_x^{-1} law although the clear k_x^{-1} law seems to be more difficult to observe as suggested by previous studies on turbulent boundary layers (Davidson *et al.* 2006).

Direct numerical simulations of a stably stratified shear layer have been widely used to assess various parameters related to turbulent mixing in the existing literature. However, most previous studies used small computational domains, where the ELSS could not grow because of confinement effects. Thus, the existence of ELSS can alter findings in previous DNS if the ELSS play important roles in the flow evolution. It was shown that the ELSS holds a large fraction of turbulent kinetic energy. This might be important from a viewpoint of turbulence modelling because the ELSS with large velocity fluctuations may affect the dissipation scaling $\varepsilon \sim \mathcal{U}^3/\mathcal{L}$ that relates the kinetic energy dissipation rate ε to the characteristic velocity and length scales, $\mathcal{U}$ and $\mathcal{L}$, of large-scale (horizontal) turbulent motions. This relation is often used in theoretical studies on stratified turbulence (Riley & Lindborg 2008; Caulfield 2021). A detailed investigation of the assumptions made in turbulence modelling should also be conducted in future studies.

Acknowledgements. The numerical simulations presented in this paper were carried out on the high-performance computing system (NEC SX-ACE) in the Japan Agency for Marine-Earth Science and Technology.

Funding. This work was partially supported by 'Collaborative Research Project on Computer Science with High-Performance Computing in Nagoya University' and by JSPS KAKENHI, grant numbers 18H01367 and 20H05754.

Declaration of interests. The authors report no conflict of interest.

https://doi.org/10.1017/jfm.2021.773 Published online by Cambridge University Press

Run		Re	Ri	Pr	N_S	L_x	L_y	L_z	N_x	N_y	N_z
1	DNS	2000	0.06	1	5	448	84	140	12 288	2304	1200
7	DNS	2000	0.06	1	16	14	4	50	384	104	320

Table 3. Computational parameters of DNS used for the assessment of the domain size effects.

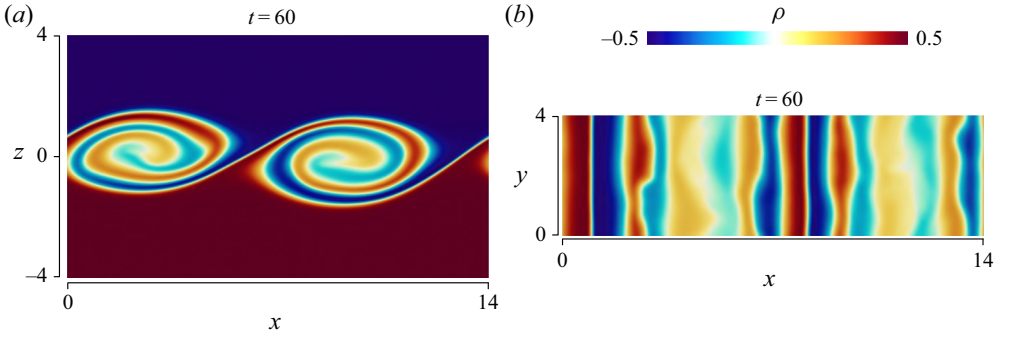


Figure 18. Density profiles on (*a*) an x–z plane and (*b*) the horizontal plane at $z = 0$ at $t = 60$ in run 7.

Author ORCIDs.
Tomoaki Watanabe https://orcid.org/0000-0002-9375-0075;
Koji Nagata https://orcid.org/0000-0002-8519-5454.

Appendix A. Effects of the computational domain size on the stably stratified shear layer

The periodic boundary condition in the horizontal direction may affect the development of a stably stratified shear layer when the computational domain is not sufficiently large. Previous studies often used a much smaller domain than present DNS and LES. In this appendix it will be shown that the small domain has non-negligible influences on both transitional and fully developed turbulent regimes of the stably stratified shear layer. We have conducted an additional DNS, run 7, for $(Re, Ri, Pr) = (2000, 0.06, 1)$ with a small computational domain as summarized in table 3. The domain size in the horizontal direction is comparable to those used in previous studies (Smyth & Moum 2000*a*; Mashayek & Peltier 2013; Kaminski & Smyth 2019; VanDine, Pham & Sarkar 2021). The grid stretching parameter is $\alpha_z = 4$ in run 7 and the spatial resolution in the shear layer is comparable in runs 1 and 7. The initial velocity perturbation is also generated by the same method for these runs. Direct numerical simulations of run 7 are repeated for $N_S = 16$ times, which are used to take ensemble averages.

Figure 18 visualizes density ρ at $t = 60$ in run 7. The streamwise length $L_x = 14$ is about twice the streamwise wavelength of the most unstable Kelvin–Helmholtz instability mode. Therefore, two roller vortices of the Kelvin–Helmholtz instability are observed in figure 18(*a*). The horizontal profile of ρ at $z = 0$ in figure 18(*b*) is almost uniform in the y direction and the quasi-two-dimensional vortices are developing at $t = 60$.

Figure 19 visualizes ρ in run 1, where panels (*b*, *d*) are taken at the same time instance ($t = 60$) as in figure 18 while (*a*,*c*) are taken at $t = 40$, at which the roller vortices of the instability are developing. In run 1 three-dimensional fluctuations have already been

https://doi.org/10.1017/jfm.2021.773 Published online by Cambridge University Press

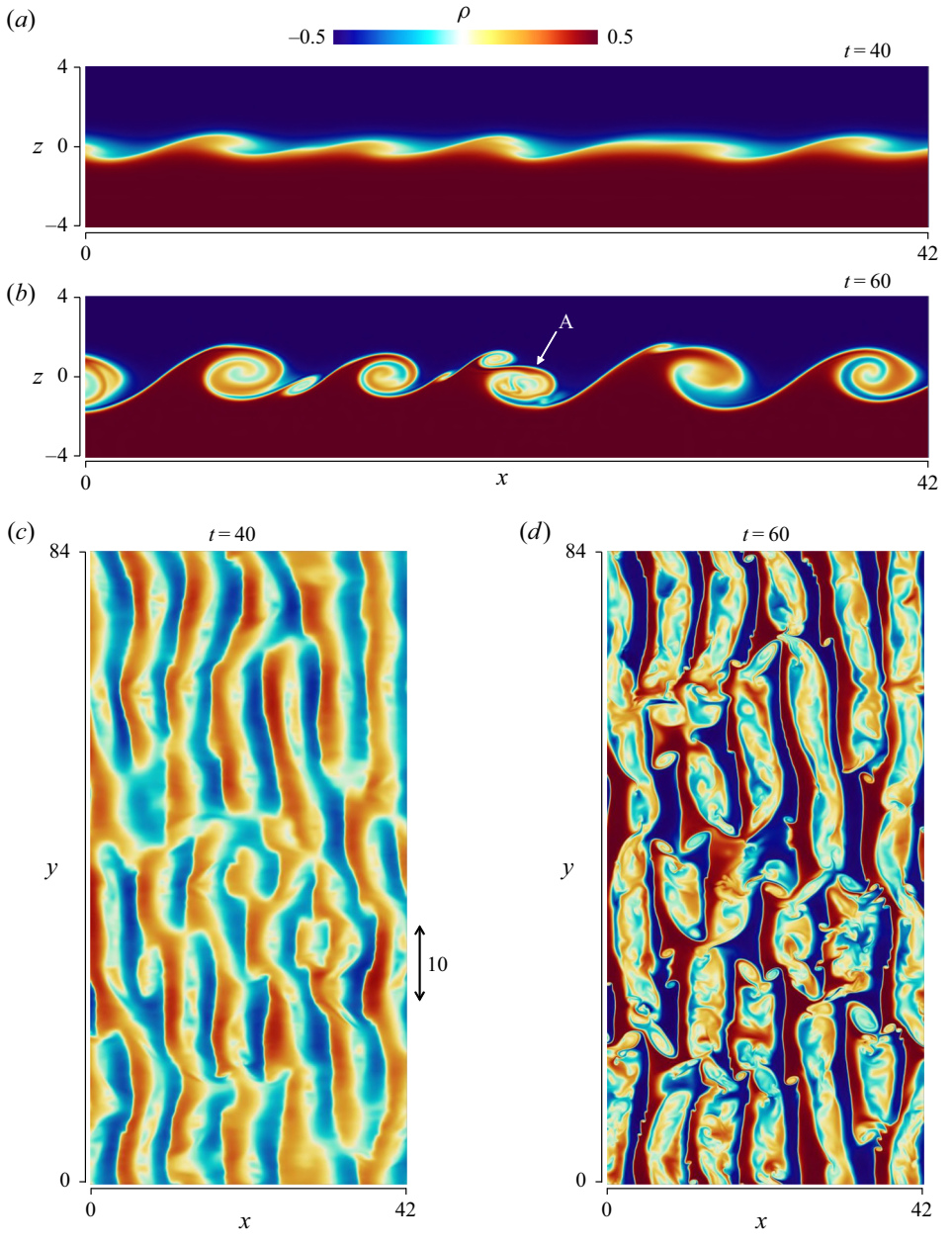


Figure 19. The same as figure 18 but for run 1: (*a*,*b*) an *x*–*z* plane; (*c*,*d*) the horizontal plane at $z = 0$. Profiles (*a*,*c*) are taken at $t = 40$ while (*b*,*d*) are at $t = 60$.

generated at $t = 60$ in the roller vortex marked as *A*. Density ρ in figure 19(*d*) also confirms the existence of three-dimensional fluctuations, which occupy a large part of the flow. Figure 20 visualizes pressure fluctuations $p' = p - \langle p \rangle$ in the same region as in figure 19. The vortex cores can be identified as negative pressure fluctuations (Taveira & da Silva 2013). The present results confirm that the vortices meander along the z direction and are not perfectly parallel to adjacent vortices. The meandering vortices of the Kelvin–Helmholtz instability were also observed in numerical simulation by Fritts

https://doi.org/10.1017/jfm.2021.773 Published online by Cambridge University Press

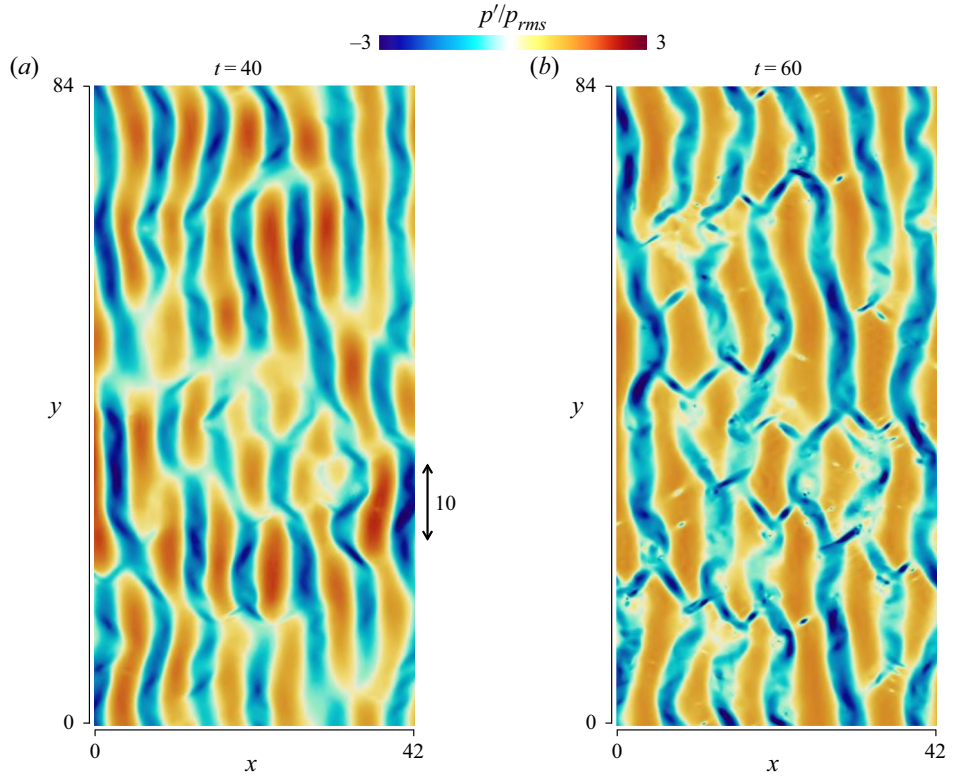


Figure 20. Pressure fluctuations $p' = p - \langle p \rangle$ normalized by the r.m.s. fluctuations p_{rms} on the horizontal plane at $z = 0$ in run 1: (*a*) $t = 40$; (*b*) $t = 60$. The same region is visualized as in figure 19.

et al. (2021). Furthermore, most vortices have a finite spanwise length even though the periodicity is assumed in the z direction. Consequently, some vortices are connected to the nearby vortices, producing highly three-dimensional density and pressure fluctuations. Figures 19 and 20 depict the non-dimensional length of 10. The characteristic spanwise length of the meandering feature of the vortices is greater than 10. Therefore, run 7 with $L_y = 4$ fails to capture this three-dimensional feature of the meandering roller vortices because the periodic boundary condition unphysically constrains the flow. The development of three-dimensional velocity fluctuations occurs faster in run 1 than in run 7. Therefore, the turbulent transition is significantly influenced by the meandering roller vortices, which are not resolved well when the spanwise domain size is small.

We also examine the effect of the domain size on the statistics of velocity and density. Figure 21(*a*) shows the temporal evolution of the shear layer thickness δ_u and the momentum thickness $I_u = \int_{-L_z/2}^{L_z/2} (1 - 4\langle u \rangle^2)\, \mathrm{d}z$ defined in Smyth & Moum (2000*b*). The shear layer thickness after $t = 100$ is smaller in run 7 than in run 1, and the shear layer growth is also influenced by the domain size. In run 1, I_u keeps increasing with t. However, I_u in run 7 tends to be constant for $100 \lesssim t \lesssim 130$ then slowly increases again. Similarly, the previous DNS whose domain size is as small as run 7 also found that I_u ceases to grow after the rapid initial increase due to the instability and then it slowly increases at a late time (Smyth & Moum 2000*b*).

Figure 21(*b*) compares the vertical profiles of $\langle u \rangle$ and $\langle \rho \rangle$ at $t = 240$ in runs 1 and 7 while figure 21(*c*) shows $\partial \langle u \rangle / \partial z$ and $\partial \langle \rho \rangle / \partial z$. Both $\langle u \rangle$ and $\langle \rho \rangle$ smoothly vary with

https://doi.org/10.1017/jfm.2021.773 Published online by Cambridge University Press

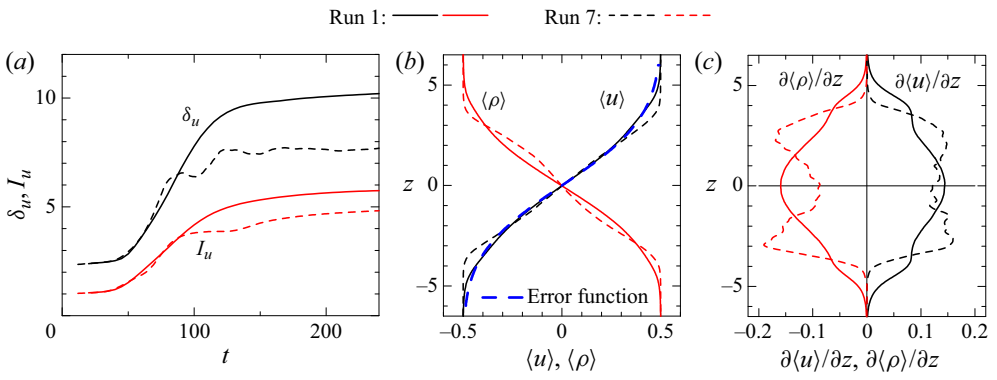


Figure 21. (*a*) Shear layer thickness δ_u and momentum thickness I_u. Vertical profiles of (*b*) mean streamwise velocity $\langle u\rangle$ and density $\langle\rho\rangle$, and (*c*) mean velocity and density gradients, $\partial\langle u\rangle/\partial z$ and $\partial\langle\rho\rangle/\partial z$, at $t = 240$.

z in run 1, and the mean velocity and density gradients become the largest at $z = 0$. In experiments by Champagne, Pao & Wygnanski (1976) the mean streamwise velocity profile in a non-stratified turbulent mixing layer is well approximated by an error function $\mathrm{erf}(X)$ as $\langle u\rangle = 0.5\,\mathrm{erf}(z/\delta_e)$ (Pope 2000). Figure 21(*b*) also shows $\langle u\rangle = 0.5\,\mathrm{erf}(z/\delta_e)$ with $\delta_e = 3.8$ and the error function is a good approximation of $\langle u\rangle$ in run 1. On the other hand, the inflection points of $\langle\rho\rangle$ appear not only at $z = 0$ but also at $|z| \approx 3$ in run 7. Therefore, $\partial\langle\rho\rangle/\partial z$ has peaks at $|z| \approx 3$. Similarly, the largest value of $\partial\langle u\rangle/\partial z$ appears at $|z| \approx 3$ in run 7. Consistently, previous studies with small domains also reported the mean velocity and density profiles similar to run 7 (Smyth & Moum 2000*a*; Mashayek & Peltier 2013; VanDine *et al.* 2021). These previous DNS are different from our DNS in terms of *Re* and initial velocity fluctuations, and the domain size effect may also be different in these studies. However, the largest gradient of $\langle u\rangle$ and $\langle\rho\rangle$ appears at $z = 0$ even in run 5 (LES) with $(Re, Ri) = (40\,000, 0.06)$, indicating that the domain size effect is similar even at higher *Re* than 2000. As also discussed below, the domain size effect found in this study is similar to that in DNS of a spatially developing turbulent mixing layer, where the initial (inflow) velocity fluctuations and the initial Reynolds number are also different from the present simulations.

Figure 22 presents the temporal variations of various statistics. Plots (*a–d*) compare the velocity and density variances in runs 1 and 7 and DNS results by Watanabe *et al.* (2017), where DNS of the stratified shear layer was performed for the same values of (Re, Ri, Pr) with $(L_x, L_y, L_z) = (48, 28, 80)$. The variances evolve with time quite differently in run 7 compared with other DNS. One of the most important differences is in the growth of $\langle v'^2\rangle$, which is significantly delayed in run 7. This can be explained by the quasi-two-dimensional roller vortices that persist for a long time because the periodic boundary condition with small L_y inhibits the three-dimensionalization of the vortices as discussed above. Direct numerical simulation by Watanabe *et al.* (2017) predicts well the initial growth of $\langle v'^2\rangle$, and $(L_x, L_y, L_z) = (48, 28, 80)$ is large enough to prevent the unphysical effects of the domain size on the turbulent transition. However, this does not mean that the domain size is sufficiently large at a late time as $(L_x, L_y, L_z) = (48, 28, 80)$ is too small for the ELSS to naturally develop. Figure 22(*e*) compares the turbulent kinetic energy dissipation rate $\varepsilon^{(k)}$ at $z = 0$ between runs 1 and 7, where the difference arising from the domain size is clear. Figure 22(*f*) presents the production $P_k = \int(-\langle u'w'\rangle\partial\langle u\rangle/\partial z)\,\mathrm{d}z$ and buoyancy flux $B_k = \int(-Ri\langle\rho'w'\rangle)\,\mathrm{d}z$ of the vertically integrated turbulent kinetic energy budget, where

https://doi.org/10.1017/jfm.2021.773 Published online by Cambridge University Press

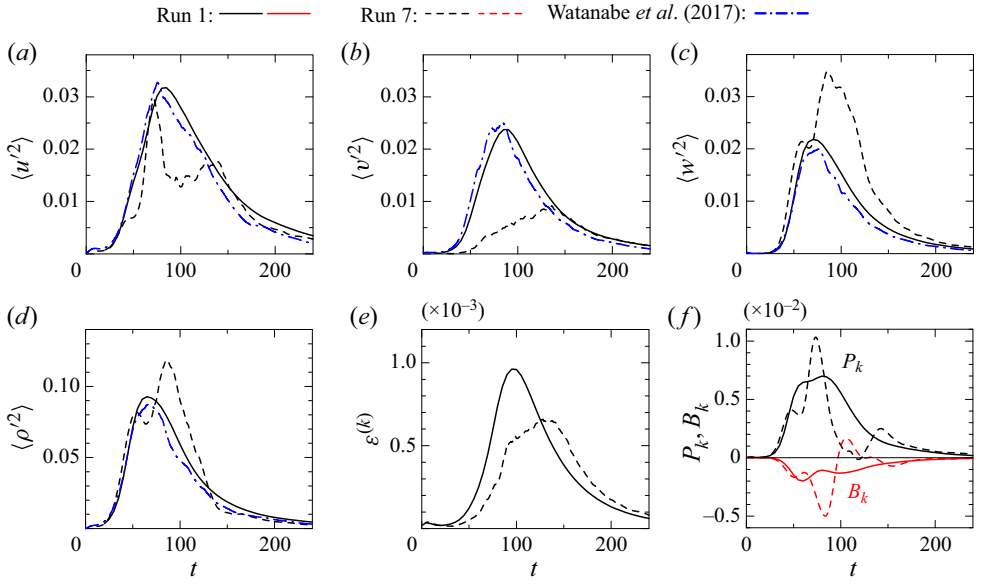


Figure 22. Temporal evolutions of statistics: variances of (*a*) streamwise velocity, (*b*) spanwise velocity, (*c*) vertical velocity, (*d*) density, (*e*) turbulent kinetic energy dissipation rate, (*f*) vertically integrated production and buoyancy flux of the turbulent kinetic energy budget. The results in (*a–e*) are taken at $z = 0$. In (*a–d*) the present DNS results are compared with DNS in Watanabe *et al.* (2017) with $(L_x, L_y, L_z) = (48, 28, 80)$.

the integral is taken from $z = -L_z/2$ to $L_z/2$. In run 1, P_k peaks at $t \approx 80$ and decreases with time while B_k also tends to decrease after the turbulent transition. Very different behaviours of these terms are found in run 7: P_k exhibits two distinct peaks at $t \approx 70$ and 140 and B_k becomes positive after the largest negative peak at $t \approx 80$. Similar temporal oscillations of P_k and B_k were reported by VanDine *et al.* (2021), where the domain size is as small as in run 7.

These results prove that the finite domain size has significant influences on the stably stratified shear layer if the domain size is as small as $(L_x, L_y, L_z) = (14, 4, 50)$. It should be noted that some previous studies tested the sensitivity of DNS to the domain size. For example, Mashayek & Peltier (2013) confirmed that doubling of the spanwise domain size from $L_y = 2$ to 4 did not affect the flow development. However, the results presented in this appendix indicate that even in the DNS with $L_y = 4$ used for their validation, the domain size was not large enough to prevent the unphysical effects of the periodic boundary conditions since the spanwise length of the meandering vortices in figure 20 is longer than 10. Thus, the findings based on the previous DNS with a small domain may need to be carefully re-examined in future works.

Finally, it should also be noted that most of these influences of the domain size are consistent with the confinement effects observed in spatially developing, non-stratified turbulent mixing layers. It was shown that the quasi-two-dimensional primary roller vortices persist for a longer time when the spanwise domain is not large enough to prevent the confinement effects (Biancofiore 2014; McMullan 2015). Flow visualization in their studies also confirmed that the interactions between meandering roller vortices lead to a fast transition to three-dimensional turbulence as also observed in this study. Furthermore, they also showed that the confinement effects in the spanwise direction suppress the growth of the momentum thickness. Similarly, the momentum thickness in

https://doi.org/10.1017/jfm.2021.773 Published online by Cambridge University Press

run 7 is smaller than in run 1 in figure 21(*a*). McMullan (2015) showed that this spanwise confinement effect on the mixing layer growth occurs for $L_y/I_u < 2.5$. Here, the definition of I_u in this study follows Smyth & Moum (2000*b*) while McMullan (2015) defined it as $\int_{-L_z/2}^{L_z/2}(0.25 - \langle u\rangle^2)\,\mathrm{d}z$, which yields 1/4 times smaller values of I_u of Smyth & Moum (2000*b*). Therefore, criterion 2.5 is different by a factor of 1/4 from that given in McMullan (2015). In this study, all DNS and LES except for run 7 satisfy $L_y/I_u > 2.5$, where the smallest value of L_y/I_u is 4 obtained at $t = 320$ in run 3 with $(Re, Ri) = (40\,000, 0)$. On the other hand, run 7 with $L_y = 4$ does not satisfy $L_y/I_u > 2.5$ after $t = 50$, and the shear layer development is strongly influenced by the spanwise confinement. The criterion $L_y/I_u > 2.5$ was obtained for spatially developing, non-stratified turbulent mixing layers, and may not be the exact value for the occurrence of the spanwise confinement in the temporally evolving, stratified shear layer. At least, it suggests that $L_y < 10$ is too small for the shear layer to naturally develop without the confinement effect.

References

Balaras, E., Piomelli, U.G.O. & Wallace, J.M. 2001 Self-similar states in turbulent mixing layers. *J. Fluid Mech.* **446**, 1–24.

Berkooz, G., Holmes, P. & Lumley, J.L. 1993 The proper orthogonal decomposition in the analysis of turbulent flows. *Annu. Rev. Fluid Mech.* **25**, 539–575.

Bernal, L.P. & Roshko, A. 1986 Streamwise vortex structure in plane mixing layers. *J. Fluid Mech.* **170**, 499–525.

Biancofiore, L. 2014 Crossover between two-and three-dimensional turbulence in spatial mixing layers. *J. Fluid Mech.* **745**, 164–179.

Bogey, C. & Bailly, C. 2009 Turbulence and energy budget in a self-preserving round jet: direct evaluation using large eddy simulation. *J. Fluid Mech.* **627**, 129–160.

Caulfield, C.P. 2021 Layering, instabilities, and mixing in turbulent stratified flows. *Annu. Rev. Fluid Mech.* **53**, 113–145.

Champagne, F.H., Pao, Y.H. & Wygnanski, I.J. 1976 On the two-dimensional mixing region. *J. Fluid Mech.* **74** (2), 209–250.

Davidson, P.A. 2004 *Turbulence: An Introduction for Scientists and Engineers*. Oxford University Press.

Davidson, P.A., Nickels, T.B. & Krogstad, P.-Å. 2006 The logarithmic structure function law in wall-layer turbulence. *J. Fluid Mech.* **550**, 51–60.

Diamessis, P.J., Spedding, G.R. & Domaradzki, J.A. 2011 Similarity scaling and vorticity structure in high-Reynolds-number stably stratified turbulent wakes. *J. Fluid Mech.* **671**, 52–95.

Fritts, D.C., Arendt, S. & Andreassen, Ø. 1998 Vorticity dynamics in a breaking internal gravity wave. Part 2. Vortex interactions and transition to turbulence. *J. Fluid Mech.* **367**, 47–65.

Fritts, D.C., Wieland, S.A., Lund, T.S., Thorpe, S.A. & Hecht, J.H. 2021 Kelvin–Helmholtz billow interactions and instabilities in the mesosphere over the Andes Lidar Observatory: 2. Modeling and interpretation. *J. Geophys. Res.: Atmos.* **126** (1), e2020JD033412.

Gargett, A.E. & Wells, J.R. 2007 Langmuir turbulence in shallow water. Part 1. Observations. *J. Fluid Mech.* **576**, 27–61.

Gerz, T. & Schumann, U. 1996 A possible explanation of countergradient fluxes in homogeneous turbulence. *Theor. Comput. Fluid Dyn.* **8** (3), 169–181.

Holt, S.E., Koseff, J.R. & Ferziger, J.H. 1992 A numerical study of the evolution and structure of homogeneous stably stratified sheared turbulence. *J. Fluid Mech.* **237**, 499–539.

Hutchins, N. & Marusic, I. 2007 Evidence of very long meandering features in the logarithmic region of turbulent boundary layers. *J. Fluid Mech.* **579**, 1–28.

Iida, O. & Nagano, Y. 2007 Effect of stable-density stratification on counter gradient flux of a homogeneous shear flow. *Intl J. Heat Mass Transfer* **50** (1–2), 335–347.

Jiménez, J. 2013 How linear is wall-bounded turbulence? *Phys. Fluids* **25** (11), 110814.

Kaminski, A.K. & Smyth, W.D. 2019 Stratified shear instability in a field of pre-existing turbulence. *J. Fluid Mech.* **862**, 639–658.

Kempf, A., Klein, M. & Janicka, J. 2005 Efficient generation of initial-and inflow-conditions for transient turbulent flows in arbitrary geometries. *Flow Turbul. Combust.* **74** (1), 67–84.

https://doi.org/10.1017/jfm.2021.773 Published online by Cambridge University Press

KENNEDY, C.A. & CARPENTER, M.H. 1994 Several new numerical methods for compressible shear-layer simulations. *Appl. Numer. Maths* **14** (4), 397–433.

KIM, K.C. & ADRIAN, R.J. 1999 Very large-scale motion in the outer layer. *Phys. Fluids* **11** (2), 417–422.

KLAASSEN, G.P. & PELTIER, W.R. 1991 The influence of stratification on secondary instability in free shear layers. *J. Fluid Mech.* **227**, 71–106.

KOMORI, S. & NAGATA, K. 1996 Effects of molecular diffusivities on counter-gradient scalar and momentum transfer in strongly stable stratification. *J. Fluid Mech.* **326**, 205–237.

KOZUL, M., CHUNG, D. & MONTY, J.P. 2016 Direct numerical simulation of the incompressible temporally developing turbulent boundary layer. *J. Fluid Mech.* **796**, 437–472.

LEE, M. & MOSER, R.D. 2019 Spectral analysis of the budget equation in turbulent channel flows at high Reynolds number. *J. Fluid Mech.* **860**, 886–938.

LEE, M.J., KIM, J. & MOIN, P. 1990 Structure of turbulence at high shear rate. *J. Fluid Mech.* **216**, 561–583.

LIENHARD, J.H. & VAN ATTA, C.W. 1990 The decay of turbulence in thermally stratified flow. *J. Fluid Mech.* **210**, 57–112.

MAHRT, L. 1999 Stratified atmospheric boundary layers. *Boundary-Layer Meteorol.* **90** (3), 375–396.

MASHAYEK, A. & PELTIER, W.R. 2012 The 'zoo' of secondary instabilities precursory to stratified shear flow transition. Part 1. Shear aligned convection, pairing, and braid instabilities. *J. Fluid Mech.* **708**, 5–44.

MASHAYEK, A. & PELTIER, W.R. 2013 Shear-induced mixing in geophysical flows: does the route to turbulence matter to its efficiency? *J. Fluid Mech.* **725**, 216–261.

MCMULLAN, W.A. 2015 Spanwise domain effects on the evolution of the plane turbulent mixing layer. *Intl J. Comput. Fluid Dyn.* **29** (6–8), 333–345.

MILES, J.W. 1961 On the stability of heterogeneous shear flows. *J. Fluid Mech.* **10** (4), 496–508.

MIZUNO, Y. 2016 Spectra of energy transport in turbulent channel flows for moderate Reynolds numbers. *J. Fluid Mech.* **805**, 171–187.

MONTY, J.P., HUTCHINS, N., NG, H.C.H., MARUSIC, I. & CHONG, M.S. 2009 A comparison of turbulent pipe, channel and boundary layer flows. *J. Fluid Mech.* **632**, 431–442.

MORINISHI, Y., LUND, T.S., VASILYEV, O.V. & MOIN, P. 1998 Fully conservative higher order finite difference schemes for incompressible flow. *J. Comput. Phys.* **143** (1), 90–124.

NICKELS, T.B., MARUSIC, I., HAFEZ, S. & CHONG, M.S. 2005 Evidence of the k_1^{-1} law in a high-Reynolds-number turbulent boundary layer. *Phys. Rev. Lett.* **95** (7), 074501.

PELTIER, W.R. & CAULFIELD, C.P. 2003 Mixing efficiency in stratified shear flows. *Annu. Rev. Fluid Mech.* **35** (1), 135–167.

PERRY, A.E. & CHONG, M.S. 1982 On the mechanism of wall turbulence. *J. Fluid Mech.* **119**, 173–217.

PHAM, H.T. & SARKAR, S. 2010 Transport and mixing of density in a continuously stratified shear layer. *J. Turbul.* **11**, N24.

POPE, S.B. 2000 *Turbulent Flows*. Cambridge University Press.

RAHMANI, M., LAWRENCE, G.A. & SEYMOUR, B.R. 2014 The effect of Reynolds number on mixing in Kelvin–Helmholtz billows. *J. Fluid Mech.* **759**, 612–641.

REDFORD, J.A., LUND, T.S. & COLEMAN, G.N. 2015 A numerical study of a weakly stratified turbulent wake. *J. Fluid Mech.* **776**, 568–609.

RILEY, J.J. & LINDBORG, E. 2008 Stratified turbulence: a possible interpretation of some geophysical turbulence measurements. *J. Atmos. Sci.* **65** (7), 2416–2424.

ROGERS, M.M. & MOSER, R.D. 1994 Direct simulation of a self-similar turbulent mixing layer. *Phys. Fluids* **6** (2), 903–923.

SALEHIPOUR, H. & PELTIER, W.R. 2015 Diapycnal diffusivity, turbulent Prandtl number and mixing efficiency in Boussinesq stratified turbulence. *J. Fluid Mech.* **775**, 464–500.

SAVILL, A.M. 1987 Recent developments in rapid-distortion theory. *Annu. Rev. Fluid Mech.* **19** (1), 531–573.

DA SILVA, C.B. & PEREIRA, J.C.F. 2008 Invariants of the velocity-gradient, rate-of-strain, and rate-of-rotation tensors across the turbulent/nonturbulent interface in jets. *Phys. Fluids* **20** (5), 055101.

SMYTH, W.D. & MOUM, J.N. 2000*a* Anisotropy of turbulence in stably stratified mixing layers. *Phys. Fluids* **12** (6), 1343–1362.

SMYTH, W.D. & MOUM, J.N. 2000*b* Length scales of turbulence in stably stratified mixing layers. *Phys. Fluids* **12** (6), 1327–1342.

SMYTH, W.D. & MOUM, J.N. 2012 Ocean mixing by Kelvin–Helmholtz instability. *Oceanography* **25** (2), 140–149.

SMYTH, W.D. & WINTERS, K.B. 2003 Turbulence and mixing in Holmboe waves. *J. Phys. Oceanogr.* **33** (4), 694–711.

https://doi.org/10.1017/jfm.2021.773 Published online by Cambridge University Press

STRANG, E.J. & FERNANDO, H.J.S. 2001 Entrainment and mixing in stratified shear flows. *J. Fluid Mech.* **428**, 349–386.

TAI, Y., WATANABE, T. & NAGATA, K. 2020 Implicit large eddy simulation of passive scalar transfer in compressible planar jet. *Intl J. Numer. Meth. Fluids* **93** (4), 1–16.

TAKAHASHI, M., IWANO, K., SAKAI, Y. & ITO, Y. 2019 Three-dimensional visualization of destruction events of turbulent momentum transfer in a plane jet. *Phys. Fluids* **31** (10), 105114.

TAKAMURE, K., ITO, Y., SAKAI, Y., IWANO, K. & HAYASE, T. 2018 Momentum transport process in the quasi self-similar region of free shear mixing layer. *Phys. Fluids* **30** (1), 015109.

TANAKA, S., WATANABE, T. & NAGATA, K. 2019 Multi-particle model of coarse-grained scalar dissipation rate with volumetric tensor in turbulence. *J. Comput. Phys.* **389** (15), 128–146.

TAVEIRA, R.R. & DA SILVA, C.B. 2013 Kinetic energy budgets near the turbulent/nonturbulent interface in jets. *Phys. Fluids* **25**, 015114.

TAYLOR, J.R., DE BRUYN KOPS, S.M., CAULFIELD, C.P. & LINDEN, P.F. 2019 Testing the assumptions underlying ocean mixing methodologies using direct numerical simulations. *J. Phys. Oceanogr.* **49** (11), 2761–2779.

THORPE, S.A. 1978 The near-surface ocean mixing layer in stable heating conditions. *J. Geophys. Res.* **83** (C6), 2875–2885.

THORPE, S.A. 2012 On the Kelvin–Helmholtz route to turbulence. *J. Fluid Mech.* **708**, 1–4.

VANDINE, A., PHAM, H.T. & SARKAR, S. 2021 Turbulent shear layers in a uniformly stratified background: DNS at high Reynolds number. *J. Fluid Mech.* **916**, A42.

WATANABE, T., RILEY, J.J. & NAGATA, K. 2016*a* Effects of stable stratification on turbulent/nonturbulent interfaces in turbulent mixing layers. *Phys. Rev. Fluids* **1** (4), 044301.

WATANABE, T., RILEY, J.J. & NAGATA, K. 2017 Turbulent entrainment across turbulent-nonturbulent interfaces in stably stratified mixing layers. *Phys. Rev. Fluids* **2** (10), 104803.

WATANABE, T., RILEY, J.J., NAGATA, K., MATSUDA, K. & ONISHI, R. 2019*a* Hairpin vortices and highly elongated flow structures in a stably stratified shear layer. *J. Fluid Mech.* **878**, 37–61.

WATANABE, T., RILEY, J.J., NAGATA, K., ONISHI, R. & MATSUDA, K. 2018 A localized turbulent mixing layer in a uniformly stratified environment. *J. Fluid Mech.* **849**, 245–276.

WATANABE, T., SAKAI, Y., NAGATA, K. & ITO, Y. 2016*b* Large eddy simulation study of turbulent kinetic energy and scalar variance budgets and turbulent/non-turbulent interface in planar jets. *Fluid Dyn. Res.* **48** (2), 021407.

WATANABE, T., DA SILVA, C.B. & NAGATA, K. 2020 Scale-by-scale kinetic energy budget near the turbulent/nonturbulent interface. *Phys. Rev. Fluids* **5** (12), 124610.

WATANABE, T., ZHANG, X. & NAGATA, K. 2019*b* Direct numerical simulation of incompressible turbulent boundary layers and planar jets at high Reynolds numbers initialized with implicit large eddy simulation. *Comput. Fluids* **194**, 104314.

WINGSTEDT, E.M.M., FOSSUM, H.E., PETTERSSON REIF, B.A. & WERNE, J. 2015 Anisotropy and shear-layer edge dynamics of statistically unsteady, stratified turbulence. *Phys. Fluids* **27** (6), 065106.

WU, X. & MOIN, P. 2009 Direct numerical simulation of turbulence in a nominally zero-pressure-gradient flat-plate boundary layer. *J. Fluid Mech.* **630**, 5–41.

https://doi.org/10.1017/jfm.2021.773 Published online by Cambridge University Press